INSTITUTO POLITÉCNICO DE BRAGANÇA Escola Superior de Tecnologia e Gestão

UTFPR UNIVERSIDADE TECNOLÓGICA FEDERAL DO PARANÁ

Modeling the natural convection in a solar dehydrator

Paulo Bruno Rossi da Silva

A thesis presented for the degree of
Master in Mechanical Engineering

As part of the dual degree program at UTFPR-CP, Universidade Tecnológica Federal do Paraná, Cornélio Procópio

Supervisors
Prof. Dr. Luís Manuel Frölén Ribeiro
Prof. Dr. Emillyn Ferreira Trevisani Olivio

Bragança
2024

This page has been intentionally left blank.

INSTITUTO POLITÉCNICO DE BRAGANÇA Escola Superior de Tecnologia e Gestão

UTFPR UNIVERSIDADE TECNOLÓGICA FEDERAL DO PARANÁ

Modeling the natural convection in a solar dehydrator

Paulo Bruno Rossi da Silva

A thesis presented for the degree of
Master in Mechanical Engineering

As part of the dual degree program at UTFPR-CP, Universidade Tecnológica Federal do Paraná, Cornélio Procópio

Supervisors
Prof. Dr. Luís Manuel Frölén Ribeiro
Prof. Dr. Emillyn Ferreira Trevisani Olivio

Bragança
2024

This page has been intentionally left blank.

Dedication

I dedicate this dissertation to my parents and my brother. They have supported me throughout my academic journey and I will be forever grateful.

This page has been intentionally left blank.

Acknowledgements

I am honored to thank my supervisors, Professors Luís Ribeiro and Emillyn Olivio. To Professor Luís Ribeiro, who guided my path at IPB and taught me the ways of academic research. To Professor Emillyn Olivio, who has been advising and supporting me since my first year at the University.

My special thanks go to my colleagues Bernardo Farrero and Nickolas Giacomitti for their help with the work and formatting of this document.

To the countless other colleagues, whose full mention would make this section too long, my most sincere thank you! There are few things in life that we don't depend on other people for, and I am glad that I can count on such dear friends for the ones we do depend on others.

This page has been intentionally left blank.

Abstract

This study presents a computational model of natural convection in a solar food dehydrator, particularly acorns, by leveraging solar energy. Solar drying offers a sustainable, low-cost alternative to conventional drying methods, which rely on high-energy inputs. By simulating the dehydrator's performance, this research aims to minimize experimental testing needs, which are constrained by seasonal and budgetary limitations. Using a three-part model (collector, chamber, and chimney), the dehydrator operates through a thermal siphon mechanism where air, heated by solar energy, flows naturally to remove moisture from the food.

The model employs Computational Fluid Dynamics (CFD) using ANSYS Fluent to simulate temperature, velocity, and flow rate conditions, validated against experimental data from tests conducted in Carrascal, Portugal. Findings show that the natural convection mechanism alone generates limited internal air movement, insufficient for consistent drying across seasons. Thus, forced ventilation was introduced, resulting in significant performance improvements with up to 3.8 times increased air outflow in autumn and 2.4 times in summer.

Simulation data, processed with MATLAB and cross-referenced with experimental measurements, underscore the need for forced ventilation in solar dryers to enhance air circulation and drying rates, especially under variable solar radiation conditions. The model offers insights for optimizing solar dryer design, potentially expanding their application in energy-limited, rural environments. Future work will explore enhanced data integration and alternative solar radiation databases to improve the predictive accuracy of the model.

Keywords: solar drying, Ansys, natural convection.

This page has been intentionally left blank.

Resumo

Este estudo apresenta um modelo computacional de convecção natural num desidratador solar de alimentos, principalmente bolotas, aproveitando a energia solar. A secagem solar oferece uma alternativa sustentável e de baixo custo aos métodos de secagem convencionais, que dependem de inputs de alta energia. Ao simular o desempenho do desidratador, esta investigação visa minimizar as necessidades de testes experimentais, que são limitadas por limitações sazonais e orçamentais. Utilizando um modelo de três partes (coletor, câmara e chaminé), o desidratador funciona através de um mecanismo de sifão térmico onde o ar, aquecido pela energia solar, flui naturalmente para retirar a humidade dos alimentos.

O modelo emprega a Dinâmica de Fluidos Computacional (CFD) utilizando o ANSYS Fluent para simular as condições de temperatura, velocidade e caudal, validado contra dados experimentais de ensaios realizados em Carrascal, Portugal. Os resultados mostram que o mecanismo de convecção natural por si só gera um movimento interno limitado do ar, insuficiente para uma secagem consistente ao longo das estações. Assim, foi introduzida a ventilação forçada, resultando em melhorias significativas de desempenho com um aumento de até 3,8 vezes na saída de ar no outono e 2,4 vezes no verão.

Os dados de simulação, processados com o MATLAB e cruzados com medições experimentais, realçam a necessidade de ventilação forçada em secadores solares para melhorar a circulação do ar e as taxas de secagem, especialmente sob condições de radiação solar variável. O modelo oferece informações para otimizar o design do secador solar, expandindo potencialmente a sua aplicação em ambientes rurais com energia limitada. O trabalho futuro irá explorar a integração melhorada de dados e bases de dados alternativas de radiação solar para melhorar a precisão preditiva do modelo.

Palavras-chave: secagem solar, Ansys, convecção natural.

This page has been intentionally left blank.

Contents

1 Introduction **1**

2 Bibliography Review **3**
2.1 Theoretical Foundation . . . 3
2.1.1 Food drying . . . 3
2.1.2 Solar drying . . . 5
2.1.3 Heat transfer . . . 6
2.1.4 Radiation . . . 8
2.1.5 Numerical methods . . . 10
2.2 State of the art . . . 12

3 Methodology **15**
3.1 Equipment . . . 15
3.1.1 Construction . . . 16
3.1.2 Experimental test . . . 17
3.2 Model boundary conditions . . . 20
3.2.1 Solar data . . . 21
3.3 Ansys Workbench setup . . . 23
3.3.1 Fluent mesh . . . 23
3.3.2 Simulation parameters . . . 24
3.4 Data treatment . . . 30
3.5 Simulations . . . 31

4 Results and Discussion **33**
4.1 Results . . . 33
4.1.1 Simulated time of 12 hours . . . 33
4.1.2 Simulated time of 20 hours . . . 45
4.1.3 Experimental data . . . 47
4.1.4 Temperature gradient . . . 48
4.2 Discussion . . . 49
4.2.1 Simulated time . . . 49
4.2.2 Singularity . . . 49
4.2.3 Temperature curves . . . 53
4.2.4 Flow curves . . . 55
4.2.5 Cumulative mass . . . 57
4.2.6 Experimental × simulated data . . . 57
4.2.7 Ventilation . . . 59

5 Conclusion **61**

A Manufacturer's catalog **67**

List of Figures

2.1 Relationship between water activity and deteriorative reaction on foods. 4
2.2 Solar dryer types. 6
2.3 Solar angles. 9

3.1 CAD model. 15
3.2 Thermosiphon mechanism. 16
3.3 Prototype construction. 17
3.4 Equipment at Carrascal test site. 18
3.5 Instrumatation. 19
3.6 Application interface. 20
3.7 Coordinates used in the simulation. 21
3.8 Test site daily direct radiation. 22
3.9 Test site temperature profile. 23
3.10 Fluent launcher. 25
3.11 Fluent setup general section. 25
3.12 Fluent setup radiation section. 26
3.13 World time zones. 27
3.14 Fluent Inlet Vent settings. 28
3.15 Volume extract's southeast half. 32

4.1 Alphanumeric classification example. 33
4.2 APN12 average temperature. 34
4.3 APN12 maximum temperature. 35
4.4 SPN12 average temperature. 36
4.5 SPN12 maximum temperature. 36
4.6 AEN12 average temperature. 37
4.7 AEN12 maximum temperature. 37
4.8 APF12 average temperature. 38
4.9 APF12 maximum temperature. 38
4.10 SPF12 average temperature. 39
4.11 SPF12 maximum temperature. 39
4.12 AEF12 average temperature. 40
4.13 AEF12 maximum temperature. 40
4.14 APN12 × SPN12 mass flow. 41
4.15 APF12 × SPF12 mass flow. 41
4.16 APN12 × AEF12 mass flow. 42
4.17 APN12 × AEN12 mass flow. 42
4.18 Outlet velocities. 43
4.19 Outlet cumulative masses. 44
4.20 Inlet velocities. 44

4.21 APN20 average temperature. 46
4.22 APN20 maximum temperature. 46
4.23 SPN20 average temperature. 47
4.24 SPN20 maximum temperature. 47
4.25 Experimental data × AEN12. 48
4.26 Experimental $[\delta T/\delta z]$ × AEN12 $[\delta T/\delta z]$. 49
4.27 APN12 temperature contour timestep 90. 51
4.28 APN12 collector singularity. 52
4.29 APN12 chimney singularity. 52
4.30 Collector's mesh edge. 53
4.31 Temperature contours at six hours simulated. 54
4.32 Streamline collector study. 55
4.33 Internal velocities comparison. 60

A.1 CUI Devices catalog. 67

List of Tables

3.1 Instrumentation used in the tests. 18
3.2 Mesh characteristics. 24
3.3 New materials and properties. 28
3.4 Report definitions. 29

4.1 Delta Mass for 12 hours simulations. 45

This page has been intentionally left blank.

Symbols & Acronyms

F_b Buoyancy force.

G Solar Constant.

β Slope angle.

γ Surface azimuth angle.

θ_z Zenith angle.

ε Emissivity.

ζ Thermal expansion coefficient.

BCT Black Body Type.

CAD Computer Aided Design.

CFD Computational Fluid Dynamics.

FDM Finite Difference Method.

FEM Finite Element Method.

GMT Greenwich Mean Time.

ISD Indirect Solar Dryer.

MSD Mixed Solar Dryer.

PV photovoltaic.

PVC Polyvinyl Chloride.

PVGIS Photovoltaic Geographical Information System.

UV Ultraviolet.

Chapter 1

Introduction

In the contemporary era, the demand for food in the global agricultural production model means that countries often specialize in one or a few types of food. This and other related factors make it necessary to transport food around the world. It is necessary to apply preservation methods for the product to arrive in proper conditions with a long shelf life. An ancient method of preservation that has the potential to significantly reduce its costs is solar dehydration.

The objective of this work is to model the operation of a dehydrator powered by solar heat. The equipment used as a reference for the simulations was designed in the LandFood project. This project was funded by the "La Caixa" Foundation at the "Promove Program", in partnership with the company Landratech.

The advantage of simulating this equipment is that it reduces the need for experimental tests. Testing in this case is particularly difficult, as it can only take place between November and January. Furthermore, as the first prototype cost 5,000 euros, one would expect future prototypes to cost around the same amount. For reasons of budgetary constraints, it is impractical to create several prototypes at once to test different configurations of chimney size, collector, and other features.

For the sake of explanation, the equipment will be divided into three parts: collector, chamber and chimney. The cold air enters through the collector, is heated, passes through the chamber and exits through the chimney. The equipment works if the temperatures in the chimney are higher than in the chamber, which is the result of the thermosiphon mechanism.

The model simulates natural convection inside the equipment. It will be validated by comparing the simulations with experimental data obtained from November 2023 to December 2023 at the Carrascal farm, Alentejo, Portugal. In this experiment, solar radiation and temperatures inside the equipment were measured.

One created the model using a Computer Aided Design (CAD) geometry drawn in SolidWorks and simulated with Computational Fluid Dynamics (CFD) methods in Ansys. The reports chosen from the simulations were: Average and maximum temperatures; Average inlet and outlet velocities; Inlet and outlet flow rates; Total mass that left the system. To obtain the temperature data for the entry of the model, the Photovoltaic Geographical Information System (PVGIS) database was used. This database also provides radiation data, which, when compared with the Ansys database and the measured values, was observed that all these data differ from each other. A correction factor was used to account for this difference.

The simulations and experimental data were evaluated in two ways, using a Matlab script to generate graphs and calculate differences and the at Ansys Post tool. The results indicate that the model works to simulate natural convection. They also indicate

that it is more sensitive to inlet temperature than to radiation. The simulations showed that the internal velocities reached a magnitude of less than $0.1m/s$, which is why extra simulations were carried out with forced ventilation. Forced ventilation proved necessary in all the simulated scenarios in order to generate significant internal velocity. Because of the forced ventilation, there was a 3.8 times increase in the total mass leaving the system for autumn and a 2.4 times increase for Summer.

The results indicate that the model needs to be refined to better evaluate if the difference in temperature values is caused by the precision of the model or by construction errors on the equipment.

This work is organized into five chapters: **Chapter 1**, Introduction, where one sets the stage by contextualizing the work and outlining its primary objectives. One will delve into the background of the topic, discussing its relevance and importance in the current landscape.

Chapter 2, Bibliography Review, presents a comprehensive review of existing literature related to the field of study. It explores the most recent and significant developments in this type of technology and analysis, examining current trends, methodologies, and theoretical frameworks. By doing so, it establishes the theoretical foundation required to understand the process and identifies gaps in the existing knowledge that the work intends to fill.

Chapter 3, Methodology, details the tools, techniques, and methods employed to carry out the research. It includes the design of experiments, data collection procedures, analytical methods, and any software or equipment used.

Chapter 4, Results and Discussion, presents the findings of the research, accompanied by appropriate data representations such as graphs, tables, and charts. It not only showcases the results but also engages in a critical analysis of the observed phenomena. This involves interpreting the data, discussing how it aligns or contrasts with existing theories or studies, and exploring the implications of the findings on the field.

Chapter 5, Conclusion, summarizes the key outcomes of the work, reflecting on how the objectives outlined in the introduction have been met. It discusses the significance of the findings and their potential impact on future research or practical applications. Additionally, it offers suggestions for future work, highlighting areas where further investigation could enhance understanding or address remaining challenges.

Three publications were produced as part of this work. In chronological order: Revisiting solar dryers for small to medium production, at the 3rd International Conference on Engineering and Sustainability in the XXI Century (INCREaSE 2023), Faro, Portugal [1]; A Novel Design Approach for Solar Dehydrators, at the Fifth International Conference: CONSOLFOOD 2023, Corunâ, Spain [2]; Responsive Dehydration Sensor driven Optimization of Production Cycles in a Solar Dehydrator, at the 1st International Conference on Smart Automation & Robotics for Future Industry (SMARTINDUSTRY 2024), Lviv, Ukraine [3].

Chapter 2
Bibliography Review

This chapter covers the basic theoretical principles to understanding the work. Furthermore it presents the state of the art as current developments in computational models for solar food dehydration.

2.1 Theoretical Foundation

This section covers the theoretical concepts needed to understand the physical phenomena and the decisions made during the work.

2.1.1 Food drying

In 2018, the export value for fresh fruit and vegetables was 138 billion dollars. One fifth of these products, or 27.6 billion dollars, are lost from the producer to the end consumer, the main cause is deterioration due to microbial activity [4].

There is, therefore, a need to preserve this food as much as possible so that it has a long shelf life. The most common form of preservation is freezing, which is widely used in all areas of the food industry. One disadvantage of this method is the high energy cost, which is why alternative preservation methods are widely sought after. Among these methods is drying, which consists of removing moisture from the food to reduce water activity, which is directly linked to microbial activity.

Water activity, abbreviated as a_w, is a measure of the availability of water in a food product for microbial growth and chemical reactions. It ranges from 0 (completely dry) to 1.0 (pure water). Unlike total moisture content, which quantifies all the water present, water activity specifically assesses how much of that water is "free" or unbound and therefore available to support the growth of microorganisms like bacteria, yeasts, and molds.

Figure 2.1 shows a curve that relates the water activity to the deteriorative reaction due to microbial activity at each point. Above 0.7 water activity, which is the natural state of the acorn after harvest, there is mold, yeast or bacteria activity. Below 0.4 there is no more enzymatic activity, a state that allows for better preservation. Below 0.2, there is only lipid oxidation, and for some manufacturing processes the desired water activity is 0.08.

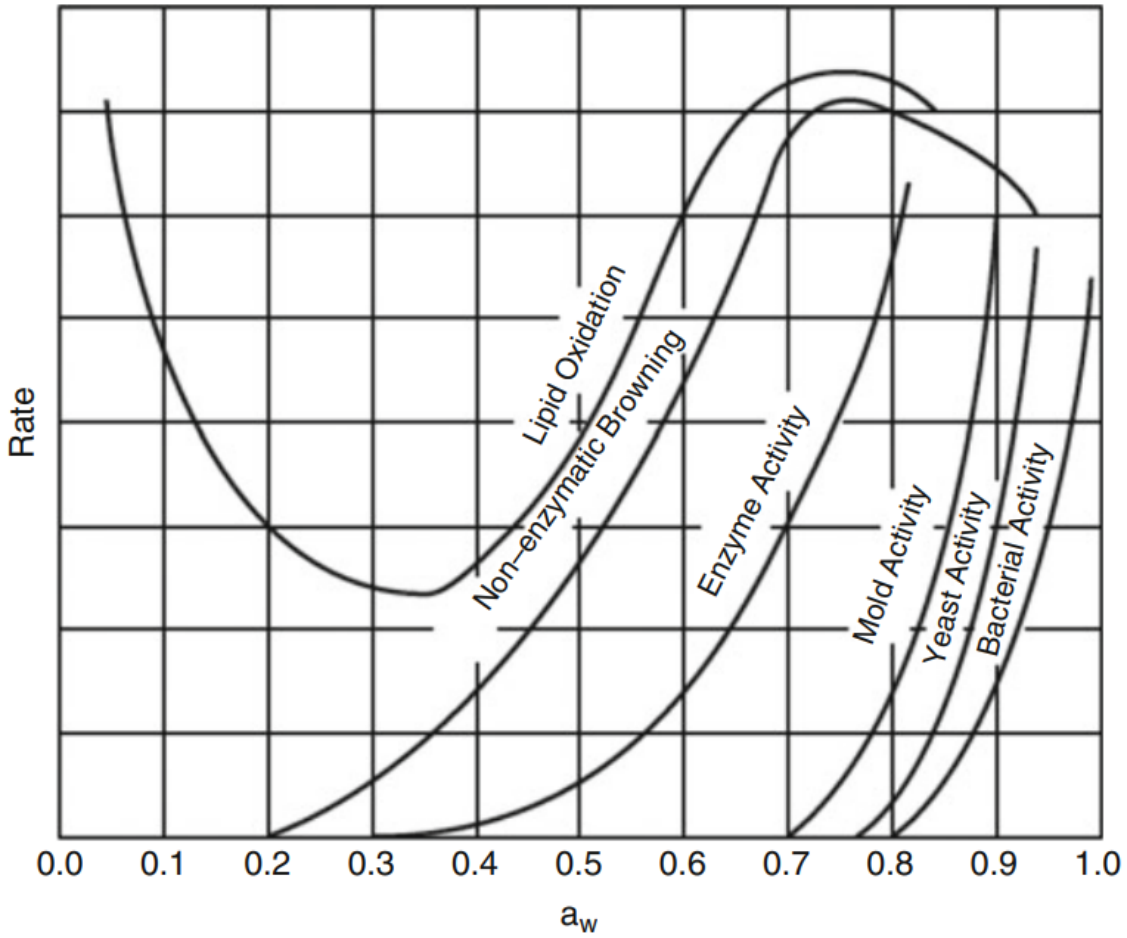

Figure 2.1: Relationship between water activity and deteriorative reaction on foods [5].

Drying is a physical method of preservation. It involves reducing the water content in food by evaporation to prevent or limit microbial growth, which requires subjecting the product to specific temperature and humidity conditions to enable mass and heat transfer. By regulating enzyme activity, which causes chemical deterioration, the shelf life of the food is extended [6]. Key factors to consider in drying include temperature, the relative humidity of the drying agent (air), and the pressure at which the process occurs.

This method can be performed either "naturally" or with the use of dryers. However, there is no uniform classification for dryers, with more than 500 different types documented [7]. A widely accepted classification is based on the technology used: Natural, Fuel-based, and Solar. Compared to Natural and Fuel, the solar type has a low investment, little product loss and, above all, lower operating costs. Since it relies solely on the sun, it does not need to be coupled to any energy source.

2.1.2 Solar drying

Solar technology dryers are devices designed for food preservation through drying, utilizing heat from solar radiation [6].

Solar drying relies on obtaining sufficient energy to increase the air temperature, which in turn lowers the air's relative humidity, enhancing its ability to absorb moisture from the product. This moisture removal is achieved through one or more components of the dryer.

As an ancient technology with limited standardization, solar dryers come in a wide variety of types, with designs ranging in complexity. Despite the lack of formal standardization, the classification into Direct Solar Dryer (DSD), Indirect Solar Dryer (ISD), and Mixed Solar Dryer (MSD) types is generally accepted.

A direct solar dryer captures solar energy to raise the air temperature via the device's roof, meaning that solar radiation not only heats the air but also directly affects the product. Ultraviolet (UV) radiation degrades the produce, leading to significant losses or reduced quality in the final product due to the deterioration of food properties, as shown in Figure 2.2 (a).

In an indirect dryer, solar radiation is used to heat the air through a dedicated component. A collector, positioned before the drying chamber, captures the solar radiation to increase the air temperature. The produce is placed inside the drying chamber, shielded from UV radiation, which minimizes or eliminates product loss, as illustrated in Figure 2.2 (b).

A mixed dryer integrates both direct and indirect drying methods. Solar radiation is collected both in the collector and through the roof of the drying chamber, allowing some UV rays to reach the product and potentially degrade the final quality, as depicted in Figure 2.2 (c) [1].

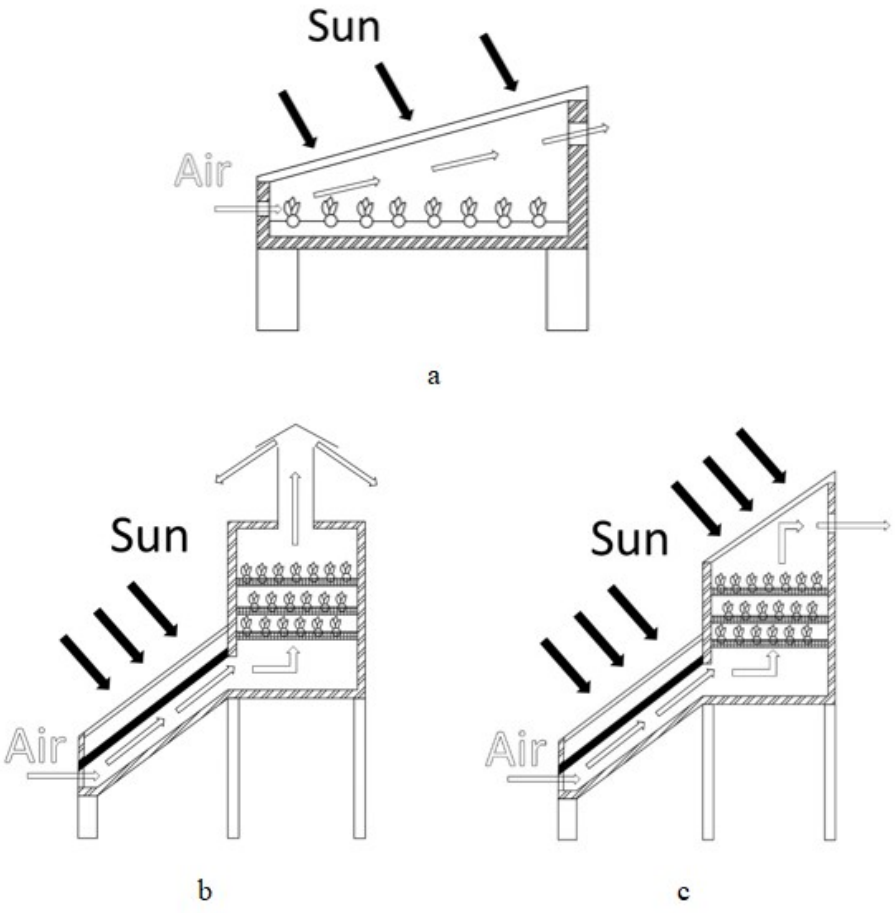

Figure 2.2: Solar dryer types [1].

2.1.3 Heat transfer

Heat transfer is the mechanism by which thermal energy moves from one place to another as a result of temperature differences. There are three types of heat transfer: conduction, convection, and radiation.

Conduction is the flow of heat through a material without any significant movement of the material itself. It occurs because of the exchange of kinetic energy between neighboring atoms. Fourier's law of heat conduction, given by Equation 2.1, states that the rate at which heat is conducted through a material is proportional to the temperature gradient and the cross-sectional area of the material.

In Equation 2.1, q is the heat transfer rate $[W]$, k is the thermal conductivity of the material $[W/m \times K]$, A is the cross-sectional area perpendicular to the heat flow $[m^2]$, $\frac{dT}{dx}$ is the temperature gradient in the direction of heat flow $[K/m]$ [8, 9].

$$q = -kA\frac{dT}{dx} \tag{2.1}$$

Convection is the transfer of heat through the movement of a fluid from one place to another and combines the effects of conduction and fluid movement. There are two

types of convection, natural and forced.

Natural Convection occurs when fluid motion is induced by buoyancy forces that result from density variations due to temperature gradients within the fluid. There are no external devices like fans or pumps to move the fluid.

Forced convection occurs when external means, such as fans or pumps, induce fluid flow over a surface or through a fluid medium to move the fluid or enhance heat transfer.

The Froude number Fr is a dimensionless parameter that is significant in the study of fluid dynamics, particularly in natural convection. It is defined as the ratio of the flow inertia to the gravitational force and is given by Equation 2.2, where v is the characteristic velocity of the flow, $g4$ is the acceleration due to gravity and L is the characteristic length scale of the system.

$$\mathrm{Fr} = \frac{v}{\sqrt{gL}} \tag{2.2}$$

The Froude number helps characterize the flow regime by comparing inertial forces to gravitational forces. A low Froude number, much smaller than one, indicates that gravitational forces dominate over inertial forces, which is typical in natural convection flows where buoyancy effects are significant [10].

The Buoyancy force (F_b) per unit volume is given by Equation 2.3, where ρ is the density of air, g is the acceleration due to gravity, Thermal expansion coefficient (ζ), T_∞ is the ambient air temperature and T_s is the surface temperature [8, 11].

$$F_b = \rho\ g\ \zeta(T_s - T_\infty) \tag{2.3}$$

Radiation is the transfer of heat through electromagnetic waves or photons, and it does not require a medium to propagate. All bodies emit thermal radiation as a function of their temperature. Thermal radiation is emitted by matter as a result of changes in the electric fields of the orbitals of atoms and the amount of radiation emitted increases with temperature.

The Stefan-Boltzmann Law, given by Equation 2.4 states that the total energy radiated per unit surface area of a blackbody is proportional to the fourth power of its absolute temperature. A blackbody is a perfect emitter and absorber of radiation, i.e. it absorbs all the radiation that reaches it and emits all its energy as radiation. However there are no actual blackbodies.

In Equation 2.4, E is the emissive power $[W/m^2]$, σ is the Stefan-Boltzmann constant ($5.670 \times 10^{-8}\ [W/m^2 \times K^4]$), T is the absolute temperature $[K]$.

$$E = \sigma T^4 \tag{2.4}$$

For real materials, i.e. not blackbodies, the Emissivity (ε) must be included, which is the amount of radiation that will be absorbed or emitted. In the law for real materials, Equation 2.5, ε varys from 0 to 1 [8, 12].

$$E = \varepsilon\sigma T^4 \tag{2.5}$$

2.1.4 Radiation

The total solar radiation can be divided in different wavelengths. One can calculate the share witch every type of radiation takes in the total solar radiation. Visible light and infrared takes the majority of it, and ultraviolet takes a small share. The Solar Constant (G) is the amount of radiation received by the earth from the sun in energy per unit of time on a unit of area. It has a constant variation through the years of 1 or 2 W/m^2. The sun subtends an angle of 32° on the Earth. The solar constant in space, without atmospheric interference is on average 1367 W/m^2 [12].

Solar radiation varies as it passes through the atmosphere, due to absorption and scattering by gases and clouds. For this reason, energy is reduced and redistributed, affecting the quality and quantity of solar radiation that reaches the surface. Solar radiation can be divided into three main types. Direct, Diffuse and Global radiation.

Direct radiation, or Beam radiation (I_b) is the radiation received without dispersion and is directional, can be focused and is useful in the application of solar concentrators. Diffuse or Indirect radiation (I_d) is that which is dispersed in the atmosphere and reaches the surface from all directions. It is less intense than direct radiation and is of great importance in cloudy situations, when direct radiation is being blocked. Global radiation (I_g) is the total radiation received by the surface, i.e. the sum of direct and diffuse radiation, given by Equation 2.6. Where $\cos\theta_z$ is the solar zenith angle. I is the total iradiation received in one hour per unit area in $[J/m^2]$. The subscripts b, d and g are beam radiation, diffuse radiation and global radiation respectively [12].

$$I_g = I_b \cos\theta_z + I_d \tag{2.6}$$

The zenith angle is the angle between the vertical and the line of direction of the sun's rays, i.e. the angle of incidence of radiation on the horizontal surface. Figure 2.3 shows many solar angles,three of which, including the zenith, will be important for this study, among which you can see a representation of Zenith angle (θ_z).

The other two relevant Figure 2.3 angles are Slope angle (β) and Surface azimuth angle (γ). The Slope angle is the angle between the surface receiving radiation and the horizontal, varying between 0° and 180° and when it is greater than 90° it means that the surface is facing the ground. The Surface azimuth angle is the deviation of the projection of the surface normal on a horizontal plane from the local meridian, measured with zero at due south, where values to the east are negative and to the west are positive

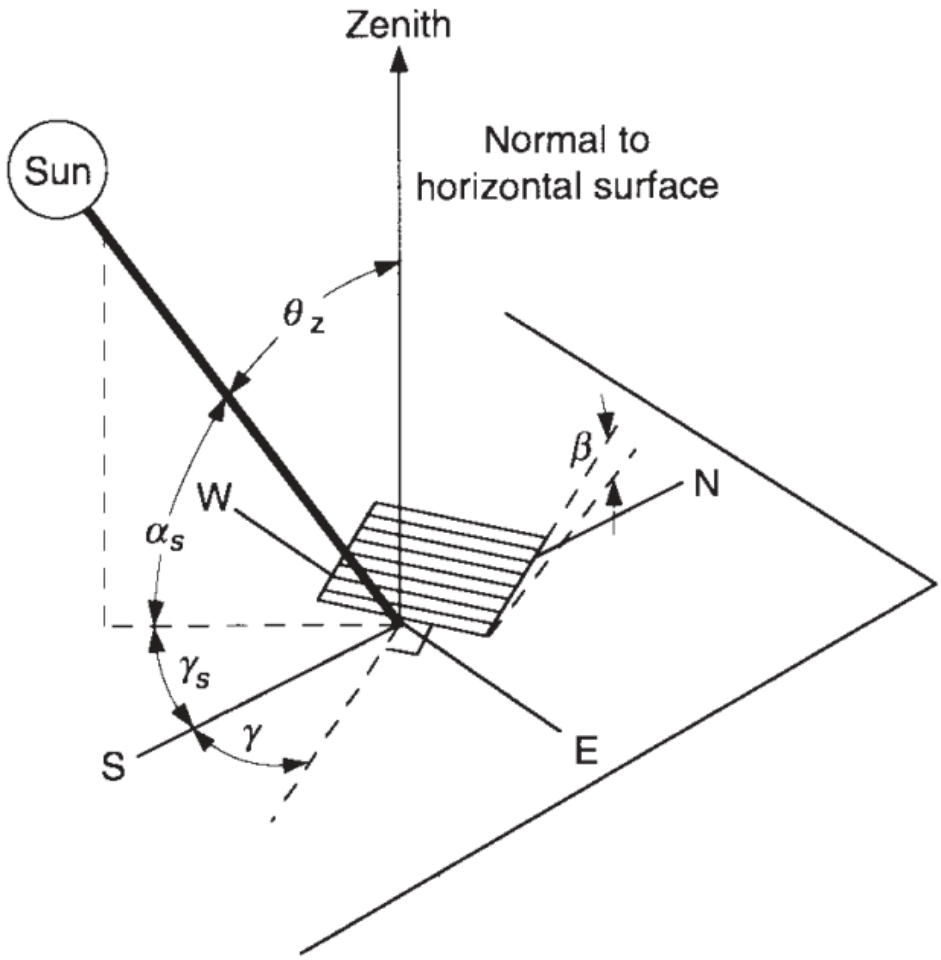

Figure 2.3: Solar angles [12].

When solar radiation is absorbed by surfaces, such as the absorber plate of a solar dehydrator, it increases the surface temperature. This elevated temperature heats the adjacent air layers through conduction. The warmer air becomes less dense due to thermal expansion, creating a buoyancy force that causes it to rise, as natural convection.

In solar dehydration, the radiation heats up an absorbing surface, which in turn heats up the air. In the case of transparent equipment, it can also act by directly heating the food, causing internal heating which helps to diffuse the moisture to the surface.

As this moisture is extracted from the food and expelled into the air, the current generated by natural convection will carry this moisture out of the equipment, allowing more moisture to escape from the food. It can therefore be said that the more radiation, the greater the natural convection and the higher the dehydration rate.

2.1.5 Numerical methods

Computational methods are a set of techniques used to solve differential equations that model physical phenomena. These methods transform differential equations into algebraic equations involving additions and subtractions that can be solved by computer algorithms. One of the most common methods is Finite Difference Method (FDM), which approximates the derivatives by finite differences using discrete values of the grid points. For example, the first derivative of a function $u(x)$ at a point x_i can be approximated using the central difference, showm in Equation 2.7 [13].

$$\left(\frac{du}{dx}\right)_{x_i} \approx \frac{u_{i+1} - u_{i-1}}{2\Delta x} \tag{2.7}$$

where Δx is the uniform distance between two grid points x_i. This approximation converts the continuous differential operator into a simple algebraic expression involving additions and subtractions of function values at neighboring points.

Another important tool is the Finite Element Method (FEM) is a powerful numerical technique utilized in CFD to solve complex problems involving fluid flow, heat transfer, and mass transfer. In FEM, the domain of interest is discretized into smaller subdomains called *elements*, over which the governing equations are formulated and solved [14, 15].

Regarding mass transfer, the conservation of mass is ensured through the continuity equation. For an incompressible fluid, the continuity is expressed in Equation 2.8

$$\nabla \cdot \mathbf{v} = 0 \tag{2.8}$$

Where $\mathbf{v}$ represents the fluid velocity vector. Within the FEM framework, this equation is applied to each element in the discretized domain. The velocity field $\mathbf{v}$, Equation 2.9 is approximated using interpolation (shape) functions N_i and nodal velocities $\mathbf{v}_i$, such that:

$$\mathbf{v} = \sum_{i=1}^{n} N_i \mathbf{v}_i \tag{2.9}$$

Where n denotes the number of nodes in an element. The continuity equation is enforced in a weak (integral) form by multiplying it with a weight function w (often chosen as the shape functions themselves) and integrating over the element volume Ω_e is presented by Equation 2.10.

$$\int_{\Omega_e} w(\nabla \cdot \mathbf{v})\, d\Omega = 0 \tag{2.10}$$

By applying the divergence theorem and incorporating boundary conditions, this integral form ensures mass conservation within each element and across the entire domain when the equations are assembled [16].

For energy transfer, particularly heat transfer, the energy conservation equation describes how energy is transported within the fluid due to conduction and convection.

The general form of the energy equation for a fluid with heat conduction and convection is in Equation 2.11.

$$\rho c_p \left(\frac{\partial T}{\partial t} + \mathbf{v} \cdot \nabla T \right) = k \nabla^2 T + Q \tag{2.11}$$

Where ρ is the fluid density, c_p is the specific heat at constant pressure, T is the temperature, k is the thermal conductivity, and Q is the volumetric heat source term. Within the FEM framework, the temperature field T is approximated using shape functions N_i and nodal temperatures T_i:

$$T = \sum_{i=1}^{n} N_i T_i \tag{2.12}$$

Substituting the approximated T and $\mathbf{v}$ into the energy equation and applying a weight function w, the weak form of the energy equation over an element Ω_e becomes the Equation 2.13 .

$$\int_{\Omega_e} w \rho c_p \left(\frac{\partial T}{\partial t} + \mathbf{v} \cdot \nabla T \right) d\Omega = \int_{\Omega_e} w (k \nabla^2 T + Q) \, d\Omega \tag{2.13}$$

After performing integration by parts and applying boundary conditions, the discretized form leads to a system of algebraic equations that relate nodal temperatures and velocities.

The discretization and solution procedure in FEM involves several steps. Initially, the domain is discretized into finite elements connected at nodes. The field variables, such as velocity $\mathbf{v}$ and temperature T, are approximated within each element using shape functions and nodal values. The governing equations are then converted into their weak forms and integrated over each element. These element equations are assembled into a global system representing the entire domain. Boundary conditions, both essential (Dirichlet) and natural (Neumann), are applied to the global system. The resulting system of algebraic equations is solved using appropriate numerical methods to obtain nodal values of velocity and temperature. Finally, the obtained nodal values are used to compute derived quantities like heat flux and mass flow rates, facilitating the analysis and visualization of the results.

As an example, consider the weak form of the energy equation after applying the Galerkin method, where the weight functions are chosen to be equal to the shape functions. The weak form is expressed as Equation 2.14 [17].

$$\int_{\Omega_e} N_i \rho c_p \left(\frac{\partial T}{\partial t} + \mathbf{v} \cdot \nabla T \right) d\Omega + \int_{\Omega_e} (\nabla N_i) \cdot (k \nabla T) \, d\Omega = \int_{\Omega_e} N_i Q \, d\Omega + \int_{\Gamma_e} N_i q'' \, d\Gamma \tag{2.14}$$

Here, N_i is the shape function associated with node i, Γ_e is the boundary of element Ω_e, and q'' is the heat flux across the boundary. This equation illustrates how the partial differential equations governing heat transfer are transformed into a set of algebraic equations involving nodal values through the application of the finite element method.

The finite element method thus provides a flexible framework for solving the mass and energy transfer equations in CFD. By discretizing the domain and approximating the field variables using shape functions, FEM converts the partial differential equations into a system of algebraic equations involving additions and subtractions. This approach accommodates complex geometries and boundary conditions, making it a valuable tool in fluid flow and heat transfer analysis [18].

2.2 State of the art

The Science Direct database was used for the state of the art. Searching three key words: solar drying, Ansys and natural convection, open access, and articles from 2018 onward were also selected. This search resulted in 122 articles, of which 26 were evaluated more detailed.

In their work [19], simulates the air and mass flow in a Mixed Solar Dryer (MSD) evaluating performance difference between two types of collectors. They indicate that 2D models are not ideal for this type of analysis, because they are not detailed enough to provide detailed airflow regimes in three dimensions.

In their study, pineapple slices were the food to be dried. To make the model simpler it was considered that the slices kept their dimensions without shrinkage. Their average element quality was maintained above 0.6 [adim.] with minimum and maximum element sizes of respectively 0.56 cm and 7.73 cm. In their study [19] chose to use an unstructured mesh. This type of meshing in CFD analysis has been vastly used for complex geometries due to its benefits [20].

The diffusivity of the food is the property that rules the drying process of said product. In Nigeria, [21] modeled the moisture diffusivity of locust beans during solar drying by forced and natural convection. In that study, it was analyzed among eleven statistical models, which fitted best their drying curve by comparing simulated with experimental data.

Their dryer configuration consisted of an Indirect Solar Dryer (ISD) with thermal storage and data acquisition systems. The equipment holds up to 40 kg of food placed in trays of $57 \times 57 \times 2$ cm. The experiments for the forced and natural convection took respectively 22 h and 28 h to reduce the initial moisture from approximately 58% to close to 7%. They concluded that the Lewis model was better to evaluated the performance of the model.

In their study [22], they developed a mathematical model to evaluate direct sun and solar drying of fermeted dairy products. The mathematical model developed made it possible to predict drying temperatures over a wide range of relative humidities and showed that air velocity has a significant impact on the moisture removal process.

The data from the mathematical model was cross-checked with experimental data from drying directly under the sun and in an ISD. The conclusion is that the solar dehydrator does not make as much difference as anticipated, and to try to justify this phenomenon he proposes three hypotheses.

During the direct sun drying process, grooves and cracks formed on the drying surface, leading to increased moisture evaporation. This effect can be attributed to the

cracks and grooves acting like fins, which expanded the surface area and consequently enhanced heat transfer.

Most of the predicted results were lower than the experimental ones, particularly under the direct sun drying system. This discrepancy may be due to the heat transfer coefficient, which remains constant only during the constant-rate period but changes during the falling-rate period. Additionally, the effect of heat conducted from the drying trays, which was not considered in the model's development, may have contributed to the differences.

Despite the lower temperatures recorded or predicted in the sun drying system compared to the solar drying temperature, moisture loss over the same drying time showed no significant differences. This can be attributed to two reasons: first, the effect of wind speed in increasing moisture loss, especially at the beginning of the drying process; second, the role of wind speed in dissipating the water vapor accumulated around the product, which creates a large vapor pressure deficit in the surrounding air, a phenomenon that did not occur in the solar drying bin.

This page has been intentionally left blank.

Chapter 3

Methodology

This chapter presents procedures and methods used to perform the experiments and simulations used during the work. It determines the model boundary conditions and the steps and configuration for simulating at Ansys Workbench software.

3.1 Equipment

The equipment is a MSD for acorns. It has been built and tested [1, 2, 3]. It has a height of 4 m, a width of 2 m and a depth of 1 m not including the collector. It has a aluminum structure covered by a tarpaulin, with sheets of insulating material on the outside bottom of the collector.

The equipment was drawn in SolidWorks, based on a model previously conceptualized by the project. The height, number of chimneys, shape, and width of the chamber were changed. The CADs of this stage can be seen in Figure 3.1, where from left to right are the folded, unfolded, and assembled models.

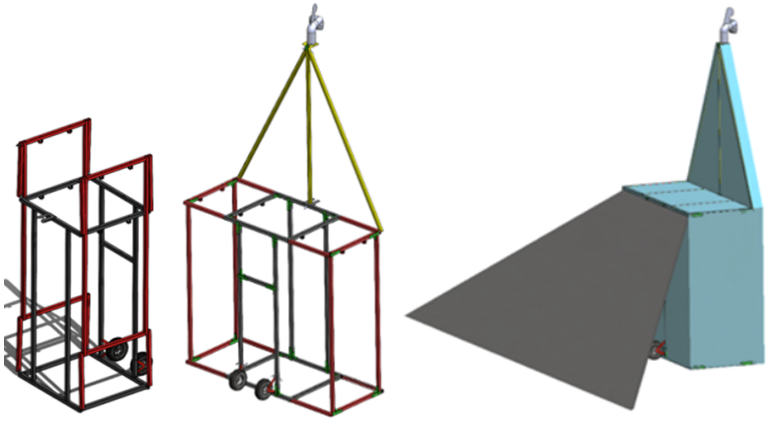

Figure 3.1: CAD model.

The equipment can be divided into three parts: collector, chamber and chimney. The collector has an area of 14 m^2. The chamber has 10.5 m^2, of which 6.4 m^2 are directly exposed to the sun. The chimney has 10.6 m^2, of which 3.6 m^2 are facing the sun. The portions of the area that are not exposed to the sun are either covered or are facing the opposite direction to the sun's rays.

The equipment works by the thermosiphon mechanism. A thermosiphon is a highly effective and straightforward method for transferring heat from one location to another

through the natural convection principle [23]. In this case, an open loop system is employed. The heat is applied to the solar collector to initiate heating. A sketch of the events sequence of this mechanism is in Figure 3.2.

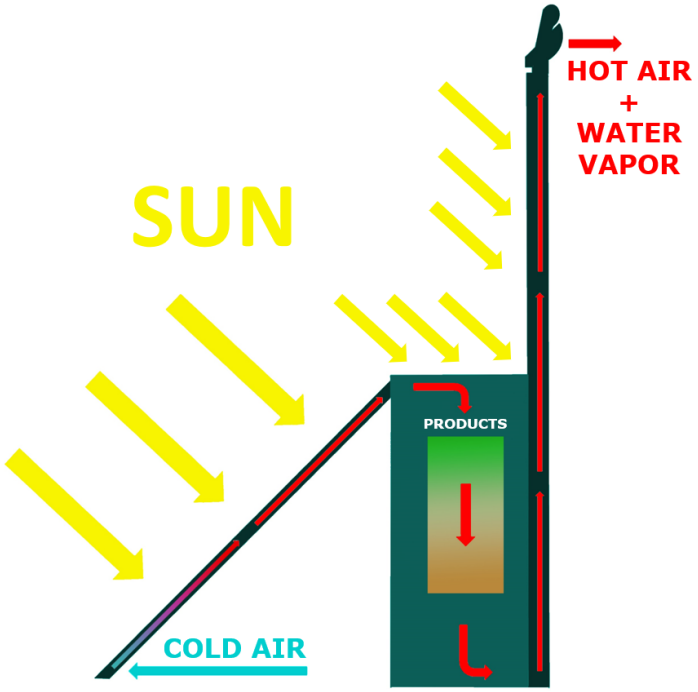

Figure 3.2: Thermosiphon mechanism [3].

The collector has an opening at its bottom chamber-faced wall. Since the collector is heated by sunlight, the air inside will increase in temperature and rise. New ambient air will enter the cavity by the differential pressure created to generate airflow.

The chamber has one opening on its top front wall where the air from the collector will enter. As the air flows inside, it will pass through the bags, carrying out the moisture as the water vapour leaves the food, the air temperature cools, increasing density. The colder air will flow to the bottom and be expelled through one opening at the bottom of the back wall.

The chimney has an opening at the bottom of its front wall, where the air from the chamber will enter. Its top part changes from a squared section to a triangular one, decreasing the area and increasing the airflow velocity. As the section area falls and the top black part is heated by sunlight, the hot air is expelled through the self-adjustable wind wheel chimney hood. This phenomena continues as long as there is a temperature difference between the heat source and its surroundings, driving the natural convection flow.

3.1.1 Construction

The folding frame was built in the IPB mechanical technology laboratory using all squares of $40 \times 40 \times 2$ mm, Figure 3.3a. The flexible 2 mm thick Polyvinyl Chloride

(PVC) tarpaulin was made by a supplier in the city of Murça, Portugal. The other structural components were purchased from local suppliers in the city of Bragança and assembled at the university. Figure 3.3b shows the equipment assembled on one of the university's properties, during one of the test periods.

(a) Aluminum structure in progress. (b) Second prototype at Quinta do Pinheiro Manso.

Figure 3.3: Prototype construction.

3.1.2 Experimental test

Experiments and tests have been carried out and published in previous studies and the information obtained in these studies will be treated in this work as experimental data [1, 2, 3].

Through a partnership between the partner company and a producer, acorns and a test site were made available. The equipment was placed there for testing during November and December 2023. Other tests were carried out previously, but without data acquisition, as they were structural integrity tests, such as at Figure 3.3b. The site provided was a farm in Carrascal, Alentejo region, Portugal, Figure 3.4.

Figure 3.4: Equipment at Carrascal test site.

The dehydrator was equipped with sensors to monitor temperature, humidity, radiation, and load. The radiation sensor is positioned on the roof of the chamber, distanced from the chimney to prevent any shading interference. The instruments that enabled the proof-of-concept validation are powered by a battery connected to a photovoltaic (PV) panel, Figure 3.4.

The PV panel ensured continuous power supply, mitigating the likelihood of data communication failures. Data collection and transmission occur via a GPRS modem. The instrumentation used in the tests is detailed in Table 3.1, and the layout of the temperature and humidity sensors is illustrated in Figure 3.5a, where each red cube marks a sensor pair. Figure 3.5b shows the initial samples placed for drying. The processing boxes for handling the measurement and communication signals can be seen on the right side of the image [3].

Table 3.1: Instrumentation used in the tests.

Measure	Reference	Quantity
Temperature/Humidity	AM2302	17
Radiation	RS-TBQ	1
Weight	300 Kg 101BH	1
Solar Panel 50/200W	-	1
GPRS modem	-	1
Monitoring System	-	1

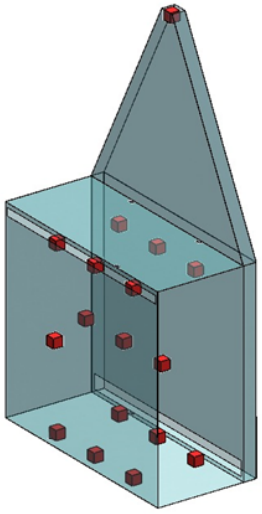

(a) Temperature and humidity sensor positioning diagram.

(b) Center – Acorn drying set-up; Right – datalogging and telemetry equipment.

Figure 3.5

The data can be tracked in real-time through a custom-built application. Figure 3.6 illustrates the main interface. On the primary screen, users can observe the temperature and humidity readings from each sensor, as well as the total product weight, which is 22.06 kg, and solar radiation at 390 W/m^2. This data allows the operator to determine when to collect the product, with notifications sent via smartphone, smartwatch, or personal computer based on the change in mass.

Temperature readings vary because the solar collector and chimney are exposed to sunlight, while the drying chamber experiences cooling through evaporation. Figure 3.6 shows the highest temperature recorded by the sensor at the top of the wind wheel chimney hood, and the lowest reading comes from the middle of the chamber. Additionally, three charts in the center present some of the daily sensor data [3].

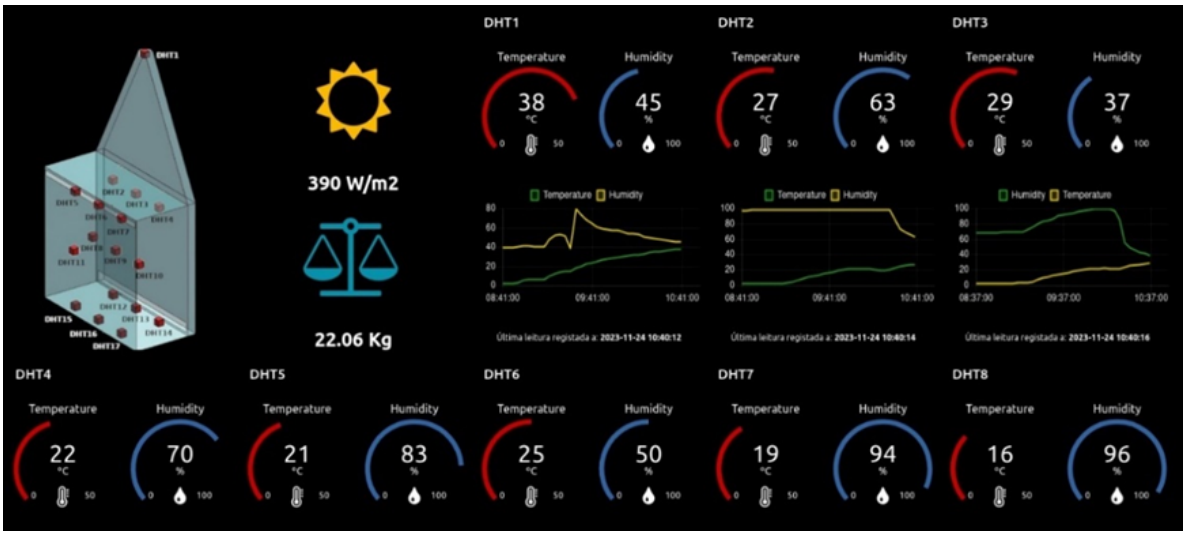

Figure 3.6: Application interface.

As the aim of this work is to simulate natural convection and air flow inside the equipment, not all the data obtained experimentally will be used. Only the measured temperatures and radiation will be considered. The implementation of mass loss analysis and humidity variations will be carried out in future work.

3.2 Model boundary conditions

To determine how the simulations would be performed, a set of boundary conditions was determined to simplify the model and standardize the analyses. These boundary conditions dictate how each part of the model behaves. In order to make the model simpler, we considered a few ideal conditions that will be described in the following.

The sides of the equipment that are not exposed to sunlight, and therefore contribute little to heat exchange, were considered perfect insulators. The malleability of the tarpaulin was disregarded, i.e. the collector geometry does not flex due to its own weight.

The geometry has been simplified by removing the metal structure from the inside. The purpose of this measure is to simplify the mesh used in the simulations. In this way, the external geometry of the equipment is maintained and the internal geometry undergoes minor changes.

For the geographical location, the coordinates to the experimental test were used. At the test site, the geographical location was acquired by the Google Maps application and subsequently applied to the PVGIS database. The coordinates were: latitude 38.449421 and longitude -8.145168. These values were obtained by the European Commission's photovoltaic geographical information platform. As indicated in Figure 3.7. where the blue localizer next to Lisbon indicates where the tests took place.

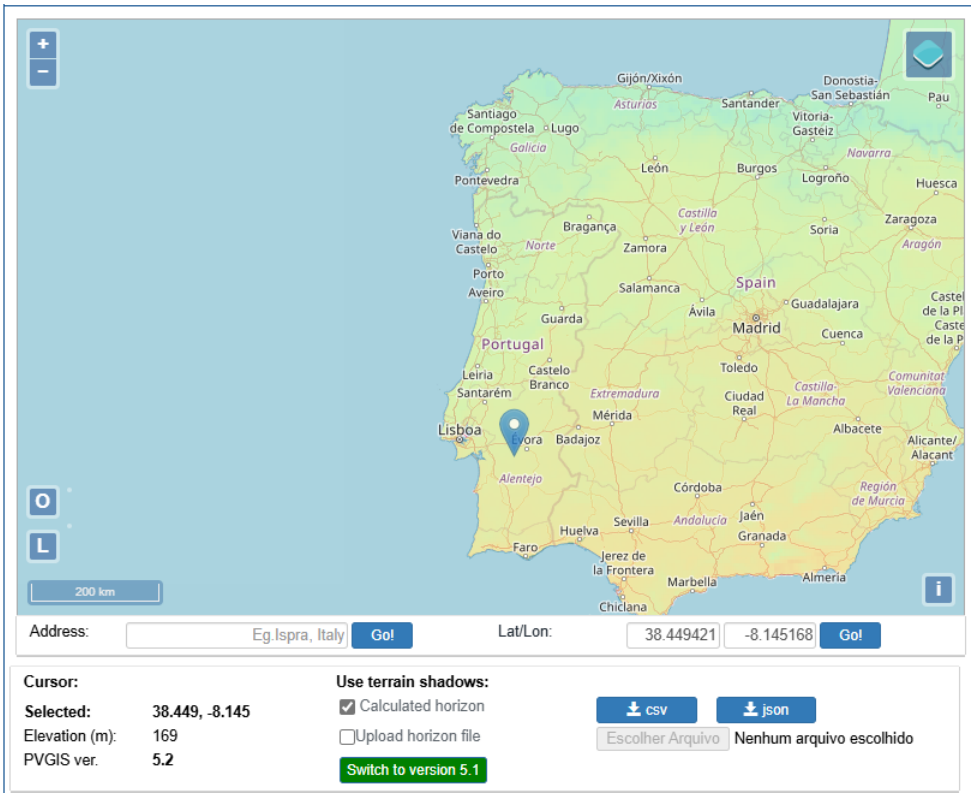

Figure 3.7: Coordinates used in the simulation [24].

3.2.1 Solar data

At PVGIS platform is possible to select exactly which data to download, such as the azimuth angle, solar tracking or fixed planes, type of radiation, monthly or daily data and form which period.

A slope angle of 45° was select since it is the collector inclination relative to the ground. The azimuth angle was set as 0°, because the collector was align with the south [12]. It was selected the daily data option, which has to be collected separately for each month, generating twelve files per location. This number can go to twenty four due to a difference from importing a PDF and the raw data. The raw data starts at midnight with one hour increments, as for the PDF starts at 45 minutes past midnight with the same one hour increment.

The raw data was used to created the temperature functions and the PDF data was used to created a visual tables where its possible to evaluate how the radiation and temperatures behave throughout the year in that location. Figure 3.8 shows the direct radiation data, from the test site. The first column represents the time of the day, the next twelve columns represents the months, where the value of each one being the radiation given in W/m^2. Cells with a value of zero means night time, without any significant solar radiation. As the radiation increases through the day and months until its maximum in August, during the summer. This increase in radiation can be easily visualized by the rise in color saturation. This allows to easily decide when is the best time to use the equipment, based on user needs. The row right after 23h45 is the daily

total radiation per square meter, this value may be useful if we need to plan how many day it would take to dry a certain amount of product based on the heat demand and the equipment efficiency.

The same process was applied to the temperature data, as seen in Figure 3.9, the colder temperatures tend to blue and the hotter to yellow. Looking at the second and last columns of both Figure 3.8 and Figure 3.9 we see that January presents lower temperatures, although it has more radiation than December, and August has the highest radiation and temperatures.

	Location: 38.449 -8.000 Database PVGIS-SARAH2				Fixed plane with slope 45° and azimuth 0°							
Hour	Direct Daily irradiance [W/m²]											
00:45	0	0	0	0	0	0	0	0	0	0	0	0
01:45	0	0	0	0	0	0	0	0	0	0	0	0
02:45	0	0	0	0	0	0	0	0	0	0	0	0
03:45	0	0	0	0	0	0	0	0	0	0	0	0
04:45	0	0	0	0	0	0	0	0	0	0	0	0
05:45	0	0	0	0	0	0	0	0	0	0	0	0
06:45	0	0	0	0	0	0	0	0	0	0	0	0
07:45	0	0	16	45	51	44	37	46	54	34	0	0
08:45	52	103	132	164	175	173	180	196	200	173	137	70
09:45	225	249	261	294	310	310	349	373	361	312	270	237
10:45	355	384	386	384	410	432	512	537	522	445	394	362
11:45	443	488	480	457	489	526	630	656	612	523	468	452
12:45	482	508	503	492	520	574	699	718	641	530	482	495
13:45	474	514	514	461	504	564	707	716	631	514	469	486
14:45	436	469	456	418	453	504	636	645	554	441	372	416
15:45	363	385	372	344	370	419	524	531	453	348	294	328
16:45	246	273	261	240	252	289	371	372	302	215	171	205
17:45	63	137	135	130	126	148	196	191	140	72	6	0
18:45	0	0	22	21	14	19	36	35	13	0	0	0
19:45	0	0	0	0	0	0	0	0	0	0	0	0
20:45	0	0	0	0	0	0	0	0	0	0	0	0
21:45	0	0	0	0	0	0	0	0	0	0	0	0
22:45	0	0	0	0	0	0	0	0	0	0	0	0
23:45	0	0	0	0	0	0	0	0	0	0	0	0
Total energy W*h/day*m²	3139	3510	3538	3450	3674	4002	4877	5016	4483	3607	3063	3051
Month	jan	fev	mar	abr	mai	jun	jul	ago	set	out	nov	dez

Figure 3.8: Test site daily direct radiation.

	Location: 38.449 -8.000 Database PVGIS-SARAH2				Fixed plane with slope 45° and azimuth 0°							
Hour	Average Temperature [°C]											
00:45	7,76	8,05	9,69	11,90	15,00	18,49	20,96	21,74	19,65	16,38	11,34	8,88
01:45	7,43	7,67	9,27	11,46	14,44	17,82	20,16	20,99	19,08	15,96	11,02	8,59
02:45	6,75	7,09	8,76	10,85	13,61	16,88	18,97	19,90	18,32	15,19	10,46	7,75
03:45	6,51	6,80	8,45	10,52	13,19	16,42	18,44	19,37	17,89	14,89	10,24	7,54
04:45	6,30	6,54	8,19	10,23	12,86	16,04	17,98	18,91	17,53	14,64	10,06	7,36
05:45	6,32	6,52	8,09	10,05	13,00	16,23	17,90	18,60	17,27	14,53	9,99	7,41
06:45	6,20	6,31	7,90	9,86	12,95	16,26	17,76	18,29	16,98	14,35	9,85	7,26
07:45	6,07	6,19	7,89	10,43	14,21	17,59	18,84	18,89	17,07	14,19	9,68	7,10
08:45	6,61	6,89	9,36	12,73	16,50	19,71	21,32	21,64	19,34	15,69	10,35	7,72
09:45	7,40	8,41	11,30	14,50	18,41	21,79	23,67	24,09	21,64	17,76	11,85	8,60
10:45	9,28	10,40	13,05	16,13	20,16	23,75	26,02	26,56	25,28	19,65	13,61	10,43
11:45	10,55	11,59	13,91	16,72	20,87	24,67	27,12	27,89	23,83	20,87	14,77	11,58
12:45	11,81	12,86	15,11	17,74	22,03	26,02	28,87	29,67	26,72	22,05	15,85	12,83
13:45	12,69	13,73	15,95	18,46	22,84	27,00	30,20	30,99	27,73	22,84	16,54	13,68
14:45	13,23	14,28	16,74	19,19	23,69	27,76	31,55	32,11	28,69	23,48	16,92	14,37
15:45	13,36	14,43	16,88	19,22	23,83	28,01	31,97	32,50	28,89	23,54	16,85	14,41
16:45	13,11	14,25	16,70	18,99	23,56	27,84	31,87	32,40	28,60	23,18	16,41	14,03
17:45	11,70	13,05	15,97	18,59	23,17	27,54	31,69	32,02	27,66	21,66	14,75	12,28
18:45	10,51	11,89	14,94	17,70	22,18	26,46	30,46	30,73	26,37	20,31	13,61	11,14
19:45	9,68	10,73	13,53	16,30	20,71	24,85	28,61	28,80	24,68	19,14	12,86	10,40
20:45	8,97	9,55	11,78	14,20	18,20	22,44	26,06	26,23	22,50	17,97	12,17	9,81
21:45	8,41	8,84	10,91	13,23	16,93	20,91	24,26	24,61	21,35	17,18	11,63	9,32
22:45	7,94	8,26	10,22	12,44	15,94	19,71	22,84	23,30	20,41	16,53	11,18	8,92
23:45	8,09	8,50	10,25	12,48	15,86	19,34	21,95	22,68	20,17	16,72	11,49	9,19
Month	jan	fev	mar	abr	mai	jun	jul	ago	set	out	nov	dez

Figure 3.9: Test site temperature profile.

3.3 Ansys Workbench setup

The software Ansys Workbench is a commonly used software in engineering analyses. It was chosen because of its features and license availability at the university. In this work version 2022 R2 was used. Fluid Flow (Fluent) was chosen.

3.3.1 Fluent mesh

Fluid Flow (Fluent) offers a separate window for editing the mesh. The mesh is a simplification of the geometry, used to calculate numerical analysis. It consists of dividing the geometry into individual elements. The smaller the elements are the closer to reality the simulation should be.

Smaller elements don't always means that a mesh with more will be adequate for

the simulation. Other factors such as the type, and method to create the elements will direct affect the mesh quality. Choosing the right method is crucial for a good simulation.

In this work many iterations were made to find the right element size. For the final simulations a size of 0.025 m was used. At first it proved to be good enough for the analysis.

To prepare the mesh, all the bodies except the extract volume were suppressed for physics. Then, using the body selection tool, the volume was selected and a sizing of 0.025 m was created. Sizing needs to be used to ensure that all elements are approximately the same size, otherwise in parts of the geometry with a lot of detail or corners, elements will be formed that are too small, increasing the complexity of the mesh, the computational cost and most of the time not improving the results. In the project tree, in the mesh branch in the defaults session, the physics preferences were set to CFD. The preference solver was set to Fluent, and the order of elements to linear.

When the mesh was ready, named selections were created. This step is crucial to configure Fluent, as it allows one to set different parameters and conditions to different faces of the mesh. In this geometry, at least four named selections need to be created, one for each air inlet and outlet, one for the faces that receive sunlight, and one for the insulation material. In order to separately evaluate the temperature, the sunlight receiving faces were split in two, the collector and the sun face. Table 3.2 shows the main mesh characteristics.

Table 3.2: Mesh characteristics.

Characteristic	Value/Option
Physics Preference	CFD
Solver Preference	Fluent
Element Order	Linear
Face sizing	0.025 m
Nodes	253249
Elements	1354247

3.3.2 Simulation parameters

The setup section is used to configure the simulation conditions. Everything from if it will consider gravity to which solution method and equations are used, it also has some report features useful to graphic visualization. Figure 3.10 shows the launcher menu, it was selected double precision, and a number of local cores equal to the total available minus one was selected as solver processes. The number of cores was chosen like that to ensure maximum performance and still keep room for basic processes from windows and other programs.

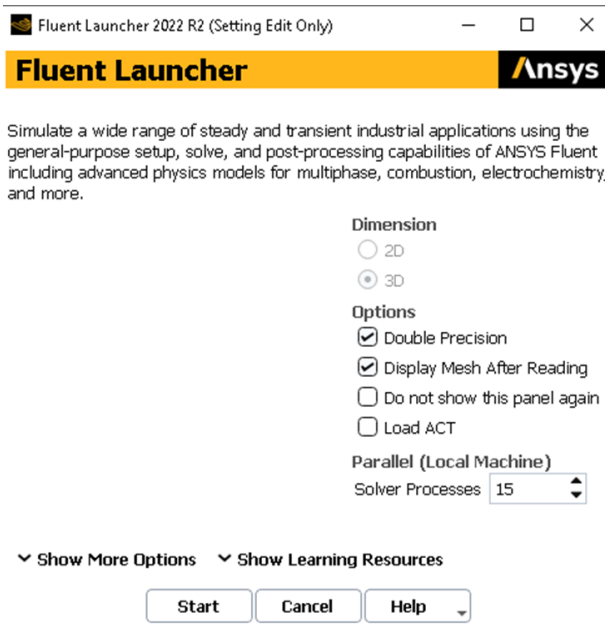

Figure 3.10: Fluent launcher.

When the setup tab opens and the mesh loads it is possible to configure the simulation. In the project tree, the first configuration is the general one, Figure 3.11, where the solver options and the type of analysis to be carried out are defined. In the type section, pressure-based was chosen, since the speeds involved are subsonic. In the velocity formulation, absolute was chosen because the reference frame will be stationary. For the time section, transient was chosen since the conditions need to vary as a function of time. As it is necessary for the density equations to work, gravity was activated and its direction and magnitude have been chosen, respectively, as $-\hat{y}$ and 9.81 m/s.

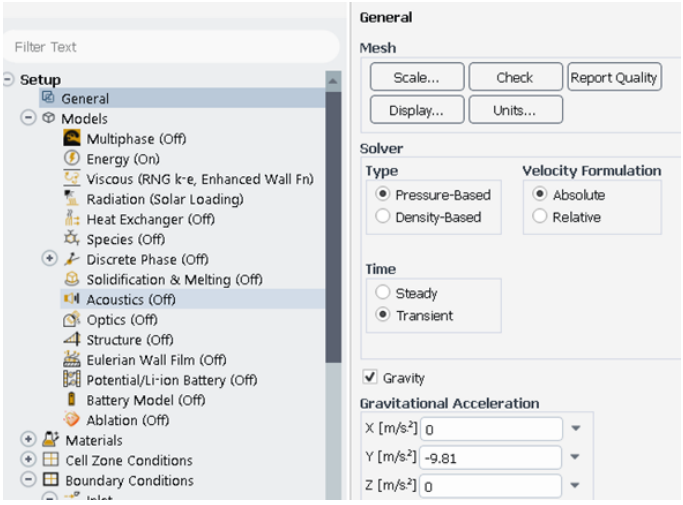

Figure 3.11: Fluent setup general section.

The next section in Figure 3.11 project tree is the models one, where only those configurations that have been changed from the defaults will be commented on. The energy equation was activated. For the viscous model it was chosen, k-epsilon (2 eqn), RNG with enhanced wall treatment, pressure gradient effects, thermal effects, and buoyancy effects set to full. The k-epsilon (2 eqn) with RNG is the most recommended model in the bibliography for natural convection due to the high computational efficiency and how it treats the buoyancy effects, crucial to convection.

The last configuration of the model section to be changed is radiation. It will be responsible for tracking radiation and solar heat. In the menu shown in Figure 3.12 one can configure various radiation models. As only natural convection by solar heat will be simulated, only Solar Load will be used, selecting the Solar Ray Tracing option. When one opens this option, the window appears in the upper right corner of Figure 3.12 appears. This new window is the solar calculator, in which is needed to choose the coordinates, time zone, and set where the north and east are.

For the geographical coordinates, the same from the experimental test were used, as mentioned above and shown in Figure 3.7. For the time zone, Greenwich Mean Time (GMT)+0 was used. As shown in Figure 3.13, the theoretical time zones run parallel to the Greenwich meridian and divide the map equally, but for geopolitical reasons countries choose to adhere to different times to those defined by the meridians, shown by the different colors. As it is necessary for the analysis of solar ray tracking to be accurate, and the radiation database cannot keep up to date with geopolitical changes, it is necessary to set the time zone according to the meridians as shown in Figure 3.13.

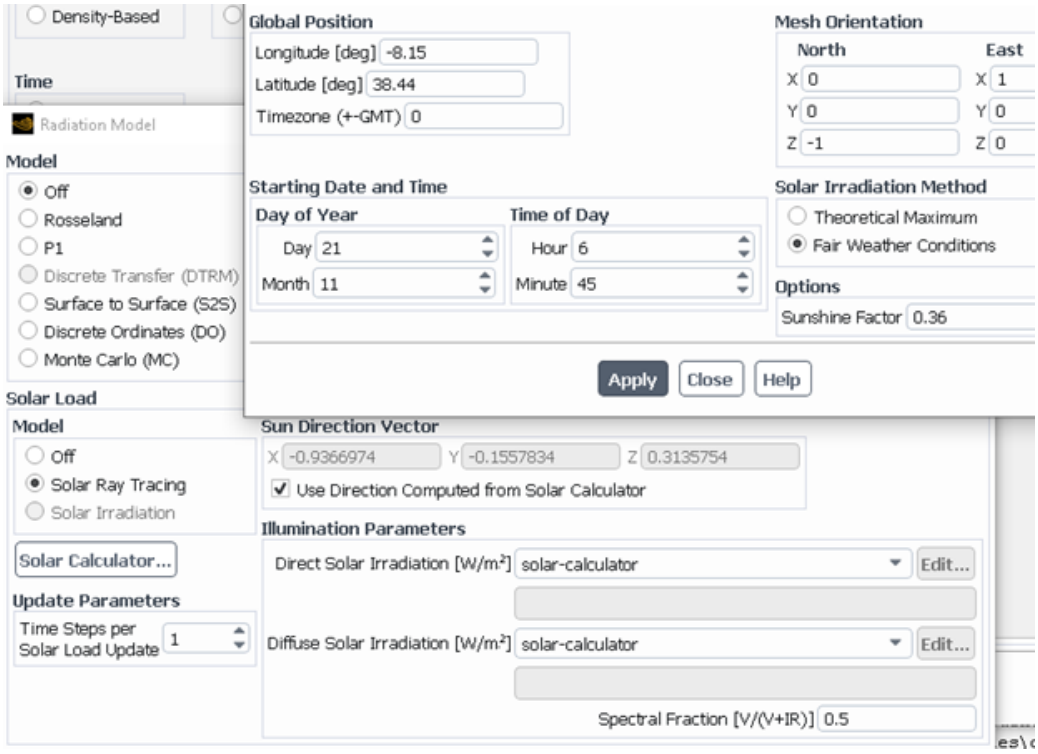

Figure 3.12: Fluent setup radiation section.

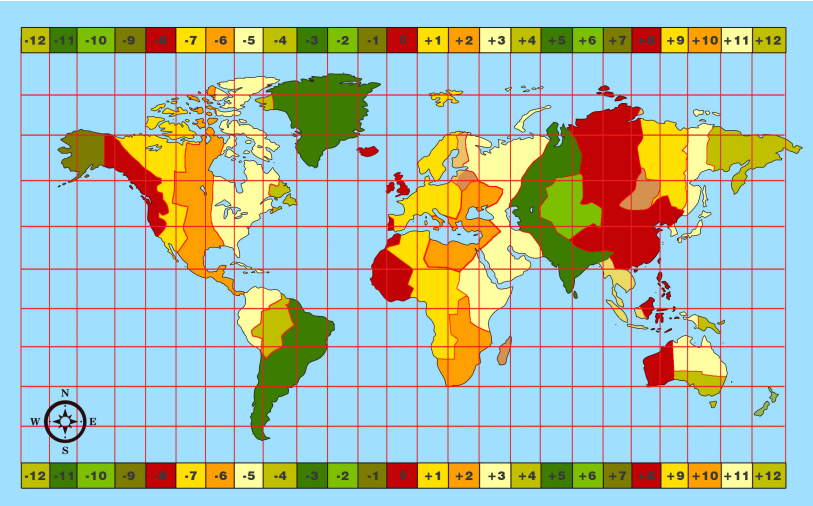

Figure 3.13: World time zones [25].

Fair weather conditions were chosen. The radiation data from the Ansys solar calculator was found to be much higher than those from PVGIS, including the autumn data from the first source being higher than the summer data from the second. For this reason, correction factors of 0.36 (PVGIS), and 0.72 (experimental data) were applied for autumn and 0.60 for summer.

Following the project tree, there is the materials section, which is divided into solids and fluids. The only fluid involved is atmospheric air, and two parameters have been changed in it, the density and the thermal expansion coefficient. The density was set to boussineq because it is commonly used in fluid dynamics, particularly in the study of buoyancy-driven flows, such as natural convection [26], with a value of 1.225 kg/m^3. The coefficient of thermal expansion was assumed to be 0.0036 K^{-1}.

When changing the density to boussineq it is necessary to go to the top, in the toolbar, in the physics section, to operating conditions and set the temperature of the boussineq parameters as the initial temperature of the system. Additionally, in the same menu, the option to specify operating density was selected and its value set to zero, so that the program can do the density calculations in a more optimized way.

For the solids, two new materials were created with the characteristics presented in Table 3.3. The properties of PVC were obtained from [27, 28] and those of the insulator were the same as before, with the exception of thermal conductivity, which was brought close to zero, to mimic a perfect insulator, the value was not set to exactly zero because it makes the simulation crash. Guides and tutorials recommend using other materials from Ansys database will be considered as insulation during the course of the work, such as ash, a material commonly used as insulation in simulations.

Table 3.3: New materials and properties.

Material	Density $[kg/m^3]$	Specific heat $[J/(kg \cdot K)]$	Thermal conductivity $[W/m \cdot K]$
PVC	1450	1000	2.5×10^{-1}
Insulation	1450	1000	1.0×10^{-7}
Ash	600	795	7.1×10^{-2}

The next part of the project tree is that of boundary conditions. In this section, properties will be assigned to each of the named selections created with the mesh. Ansys automatically detects some of the named selections, Inlet and Outlet are already predefined because of the name assigned to them. It also detects that the extract volume is a volume and the rest it assumes are walls. However, the standard inlet is not suitable for solar heat convection because it is a velocity inlet, i.e. it will always send a set velocity.

For the case under study, the inlet velocity needs to be able to vary according to the pressure difference generated by the variation in air density inside the collector as it is heated and rises towards the chamber.For the program to understand that the inlet is an opening to the outside environment, it must be configured as Inlet Vent, as shown in Figure 3.14.

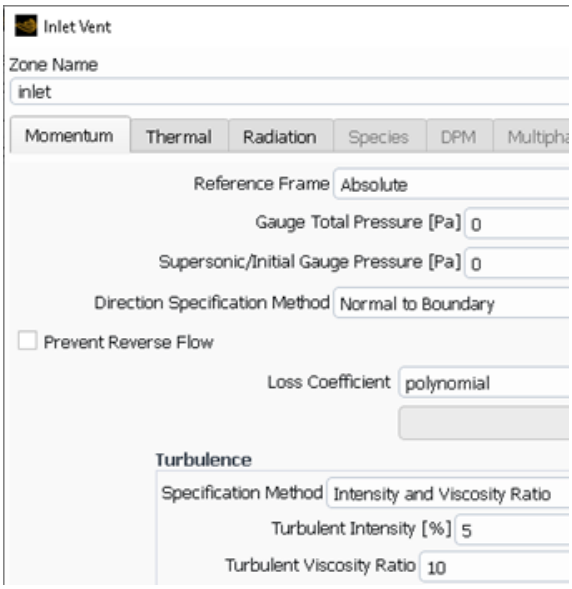

Figure 3.14: Fluent Inlet Vent settings.

In the Momentum section, everything was left at default, because there will be reverse flow at certain times and when the pressures are left at zero, the program understands that the outside pressure is atmospheric pressure. In the thermal conditions section, the temperature expression that would be used for each specific simulation was entered, which will be explained later in the project tree. For radiation,

as it is an opening, it should be defined as not participating in solar ray tracing.

The pressure outlet was left as the default since it assumes an opening to the external environment. Thus, all default momentum settings were maintained, the thermal ones were kept the same as those defined for the inlet in each simulation, and it also does not participate in the solar ray tracing.

Since there were three other named selections, they will have to be configured separately. Two of them will be of the material defined as PVC and the other as Insulating. All of them will participate in the solar ray tracking, with the difference that the insulating wall will have an absorptivity factor of 0.2 instead of 1.0 like the other two. Absorptivity defines the percentage of thermal radiation that will be retained by the wall, with 1.0 meaning all radiation is absorbed and 0.2 meaning only 20% is absorbed. In the same radiation section, it is necessary to define the Black Body Type (BCT), between opaque and semitransparent. Opaque is for materials that are not permeable to radiation, such as wood, concrete, and metals. Semi-transparent is for materials that allow a portion of the radiation to pass directly through them without being absorbed by the body, such as glass and transparent plastic [29].

In the thermal section form the boundary conditions a specific function was chosen, this function was created based on the temperature data from PVGIS for a average day in November, the same data used in Figure 3.9.

The next step is to set the data that will be recorded during the simulation. If the information is not request before the simulation stars we can‘t recover it afterwards, and a new simulation would be necessary. In the project tree In report definitions, sixteen reports were created. It is possible to chose if the reports will be ploted in real time during the simulation or not, either way the data is recorded. We can also chose to plot more than one report per chart if the units are the same, for example, the average temperature of the outlet and the inlet, and the data are still recorded separately.

In Table 3.4 in the first column are the faces to which the data relate, the following columns are the physical quantities recorded individually, where the marker × means that the data from that report was recorded.

Table 3.4: Report definitions.

Face \ Report	Average temperature $[°C]$	Max. temperature $[°C]$	Average mass flow rate $[kg/s]$	Average velocity $[m/s]$
Inlet	×	×	×	×
Outlet	×	×	×	×
Collector	×	×		
Sun Face	×	×		
Insulation	×	×		
Volume	×	×		

The data chosen to create the report files were processed using Microsoft Excel and Matlab software. The data is stored in the Ansys directory in a format called **.out**. These files contain all the data for the variables chosen in Table 3.4.

This data can be read as **.txt** by Microsoft Excel's query. The query is needed to separate the columns and transform the data so that it can be understood as numbers by Excel and the variable names can be understood as text with characters acceptable to Matlab.

Then it is necessary to initialize fluent, if there is a problem with the setup it will show a warning. In the project tree there is an initialization section and to proceed you must initialize from all zones.

Once initialization is complete, it is possible to set up some animations to visualize the equipment in action. For this study, three animations were created for each simulation, depicting different views, to observe the temperature on the surfaces of the volume, which are very close to the temperatures of the walls to which they correspond.

Finally, it is time to set the calculation conditions, where the size, quantity, and number of interactions for each time step will be chosen. The time step size was set to 300 seconds, other sizes were tested but when smaller than this they increased the simulation time and when larger they caused convergence problems due to the discrepancy between the temperature input and the radiation data.

3.4 Data treatment

The data chosen to create the report files were processed using Microsoft Excel and Matlab software. This data can be read as **.txt** by Microsoft Excel's query. The query is needed to separate the columns and transform the data so that it can be understood as numbers by Excel and the variable names can be understood as text with characters acceptable to Matlab. The Matlab script reads the Excel files directly from the computer directory and automatically plots the graphs and saves them in the same directory in .fig format, so that they can be edited without having to compile the code again.

With these data, it is possible to generate around eighty plots to evaluate the results. This number of plots is a combination of the information contained in Table 3.4 and the number of simulations of the different scenarios. Thus, it is possible, for example, to compare the average temperatures between two simulations with different parameters or even the average and maximum temperatures of a single simulation with each other.

The script will also be used to calculate differences between data from different simulations and to calculate secondary information, such as the total air volume leaving the equipment, by integrating the mass flow data as a function of time. With this information, the results will be analyzed and later discussed. In addition, the simulated data will be compared with the experimental one.

3.5 Simulations

Around one hundred simulations were performed, adding up to approximately 400 hours of computing time, of which eight of them generated data for discussion in this work. The other ones were used to fine-tune the process. They were used to build the walk-through shown in Section 3.3 and 3.4.

Due to the difficulty of the work, a large part of the time was used to come up with a reliable process for simulating natural convection. For this reason, there was no time to implement the mass transfer that occurs through the loss of humidity inside the chamber. Therefore, only natural convection and the flow of equipment with no product inside were considered .

Every simulation was made with the southeast half from the original geometry, Figure 3.15, to save in computational time. In these preliminary analyses, the collector was simulated individually 24 times. These studies served to understand how the air flow behaved within the geometry and how it influenced the temperature of the walls.

After studying the collector, it was decided that the remaining simulations would be carried out with the entire geometry, i.e. the collector, chamber and chimney assembly. It was chosen this way because importing the outlet data from the collector and accounting for the pressure loss generated by the chimney hood would take more work and simulations than a single geometry.

The next 40 simulations were to find out how the software responded to variations in different configurations and mesh sizes. Once this data had been acquired, the ten simulations that will be used to discuss the problem were carried out.

To this end, these simulations differ in four parameters: season, solar radiation, forced ventilation, and simulated time.

The season differs between summer and autumn, with August being the month with the most radiation and November being the month when the field tests were carried out.

The solar radiation alternates between the corrected radiation as mentioned in Section 3.3.2 and double that value. This was tested to see how performance changes when more heat is available, and in the autumn case to mach the experimental data.

Forced ventilation varies between having or not having the help of a fan at the chimney outlet. This was configured using the outlet pressure boundary condition, choosing a target mass flow. The amount chosen was 0.01715 kg/s of air, a value adapted from half of a commercial fan with a flow rate of 29 l/s whose frame dimensions match those of the equipment. The model chosen was the **CFM-8025BG-260-484** by *CUI Devices*, shown in Appendix A.1.

The simulated times were 12 or 20 hours. The first option was to save computational time by starting the calculation just before dawn. The second option was chosen to analyze the behavior closer to the experimental one. A 24-hour period was not chosen because it was observed that for some unidentified reason, the simulations crashed.

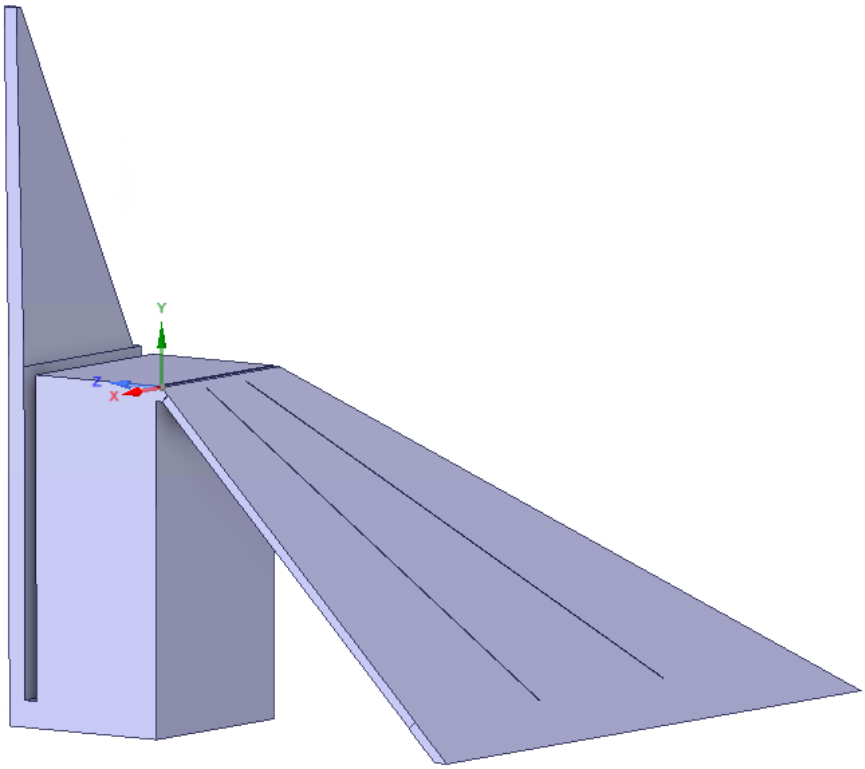

Figure 3.15: Volume extract's southeast half.

Chapter 4
Results and Discussion

This chapter presents the results of the simulations. In addition, these results will be discussed and compared to experimental data. First all the results and plots will be presented in one section and later discussed in the following section. To make it easier to distinguish between different simulations, an alphanumeric classification system will be used.

The alphanumeric classification system is made up of four slots, each representing a parameter. The first slot represents the season with **S** for summer and **A** for autumn. The second is for the amount of radiation, where **E** represents the experimental data and **P** the radiation provided by PVGIS. The next slot alternates between **F** and **N**, respectively for forced and natural ventilation. The last slot represents the simulated time and is indicated by a number in hours. Figure 4.1 it is an example, it indicates a simulation for a twenty-hour period for a autumn day, with radiation data matching the experimental, with forced circulation.

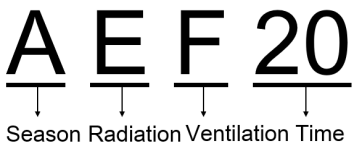

Figure 4.1: Alphanumeric classification example.

4.1 Results

The focus of this section will be to present the plots generated by the Matlab script. To help understand them, one presents values calculated from the data sets used to create these plots. They will be displayed according to the four parameters set for distinguishing the simulations.

4.1.1 Simulated time of 12 hours

As there is no experimental data for the summer, there will be no simulations that follow the **SE** _ _ pattern. Plots with only one scenario follow the same pattern, as seen in Figures 4.2 and 4.7, respectively the average and maximum temperatures for simulation **APN12**. The y-coordinate shows temperatures in degrees celsius [$^{\circ}C$] and the x-coordinate shows the elapsed time in hours [h], not time of day, i.e. the graphs do not start at midnight, but just before dawn. There are six sets of data. Pink diamonds are the Sun face data, which are the faces that receive sunlight except

for the collector. The continuous black line is the inlet air temperature, which also corresponds to the outside air temperature. The blue circles are the temperature of the outlet face. The red dashed line is the temperature of the collector walls. Green triangles are the temperature of the parts of the insulating material. The cyan asterisk is the temperature of the air volume inside the equipment.

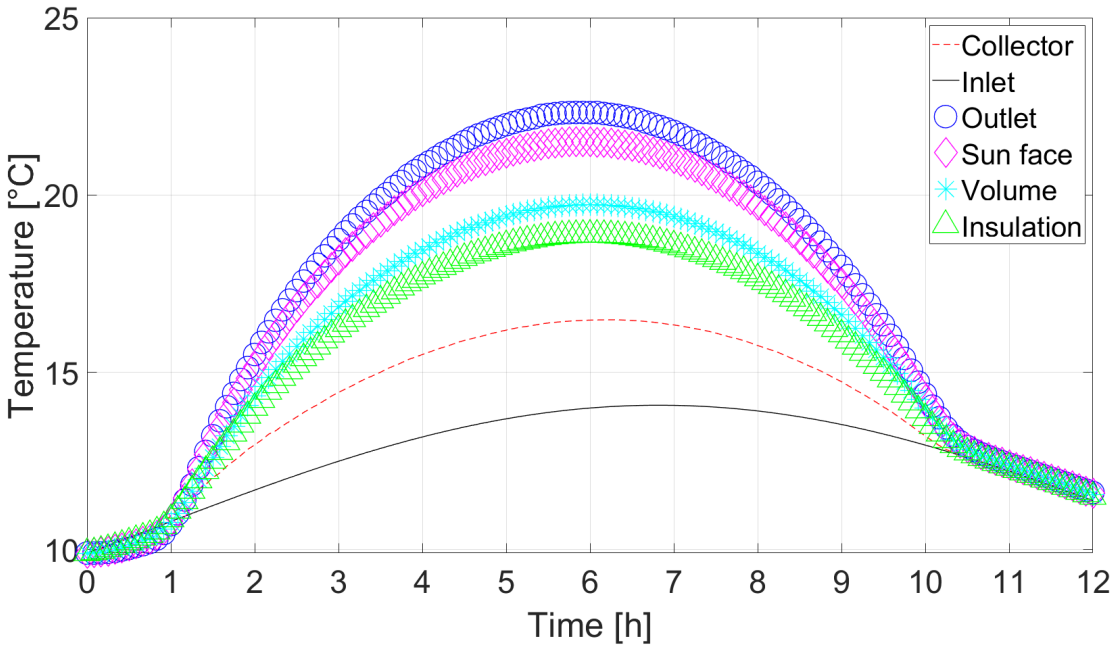

Figure 4.2: APN12 average temperature.

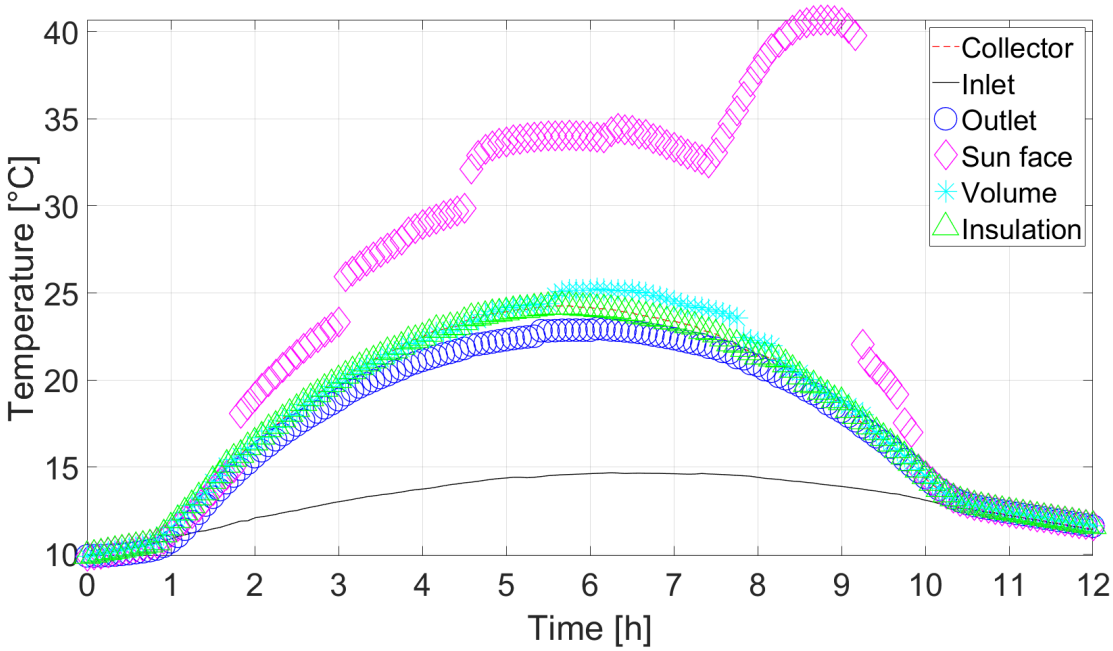

Figure 4.3: APN12 maximum temperature.

Figures 4.4 and 4.5 shows the temperatures for the summer. Since summer has more sun hours than autumn, these simulations do not show the entirety of the process, but they show the maximum of the plot.

Figures 4.6 and 4.7 shows the simulated temperatures based on the radiation measured experimentally.

Figures 4.8 and 4.9 and Figures 4.10 and 4.11 show the scenario for PVGIS radiation and forced ventilation for both seasons.

Figures 4.12 and 4.13 show the scenario of experimental radiation and forced ventilation for autumn.

Figure 4.14 compares the inlet and outlet mass flow between autumn and summer for PVGIS radiation and natural ventilation. The y-coordinate shows the mass flow rate in $[kg/s]$, where positive values means air entering the volume and negative ones, air leaving the volume. The x-coordinate just like the temperatures figures indicates simulated time in hours, starting just before dawn. The continuous black line is the inlet for **APN12** and the dashed red one is for **SPN12**. The green triangles line is the outlet for **APN12** and the blue circles, for **SPN12**.

Figure 4.15 compares the mass flow for summer and autumn for forced simulation scenario. The axis and markers work like Figure 4.14, except for the ventilation indicator from the alphanumeric system.

Figure 4.16 compares between forced and natural ventilation for autumn. The axis works like the previous figures. The continuous black line is the inlet for **APN12** and the dashed red one is for **AEF12**. The green triangles line is the outlet for **APN12** and the blue circles, for **AEF12**.

Figure 4.17 compares autumn natural ventilation simulations that vary between

PVGIS and measured radiation. Where the axis behaves as the previous figures. The continuous black line is the inlet for **APN12** and the dashed red one is for **AEN2**. The green triangles line is the outlet for **APN12** and the blue circles, for **AEN12**.

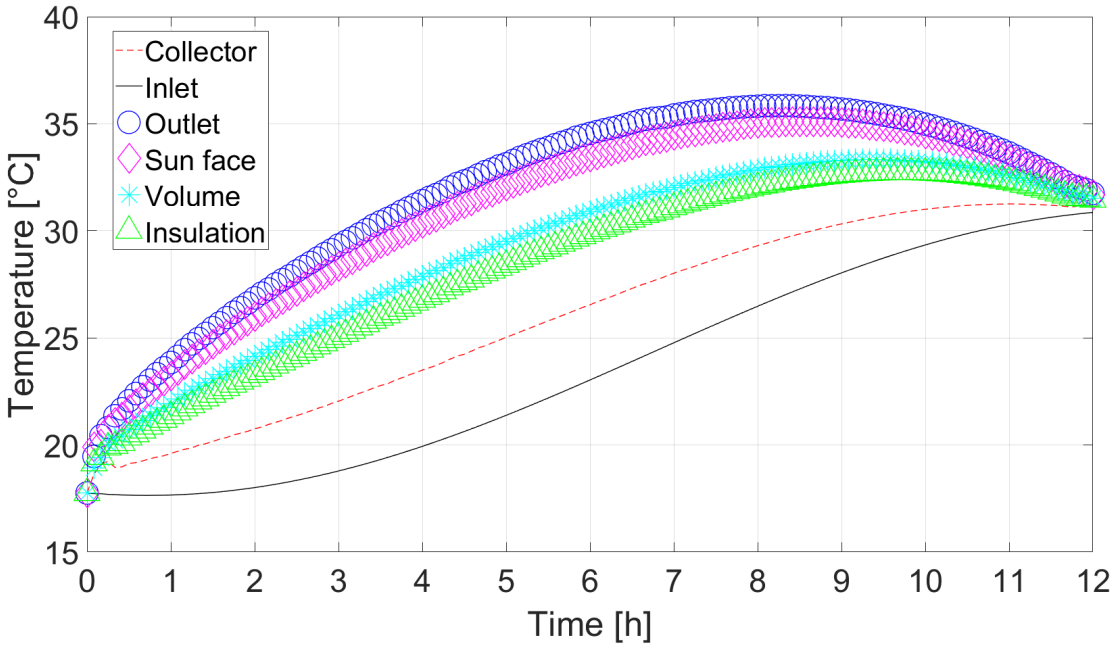

Figure 4.4: SPN12 average temperature.

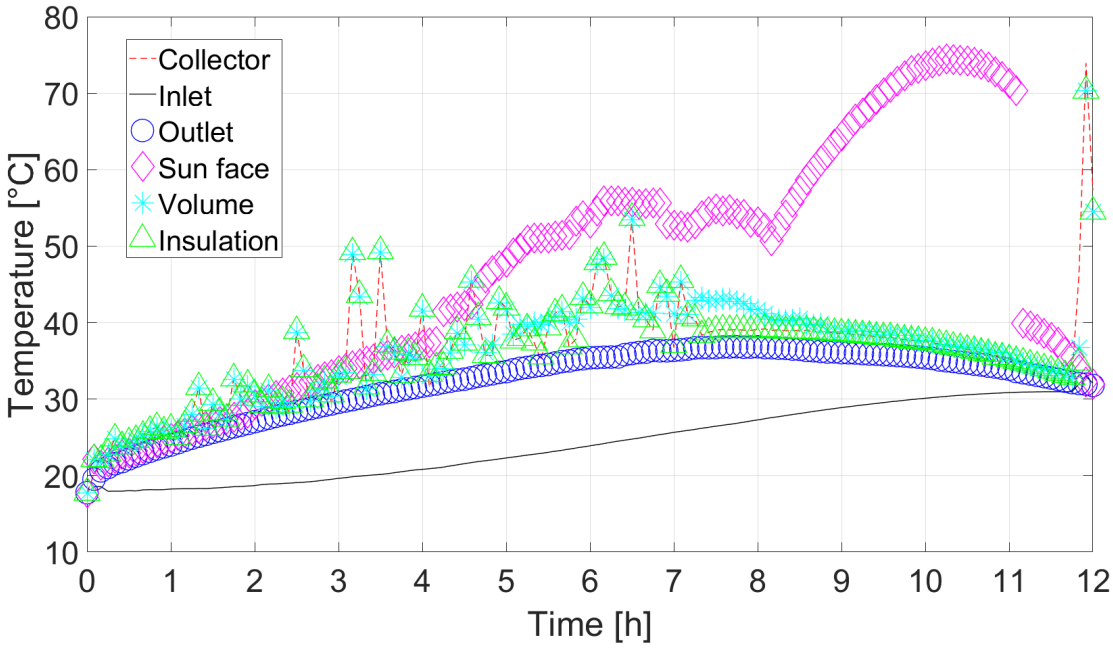

Figure 4.5: SPN12 maximum temperature.

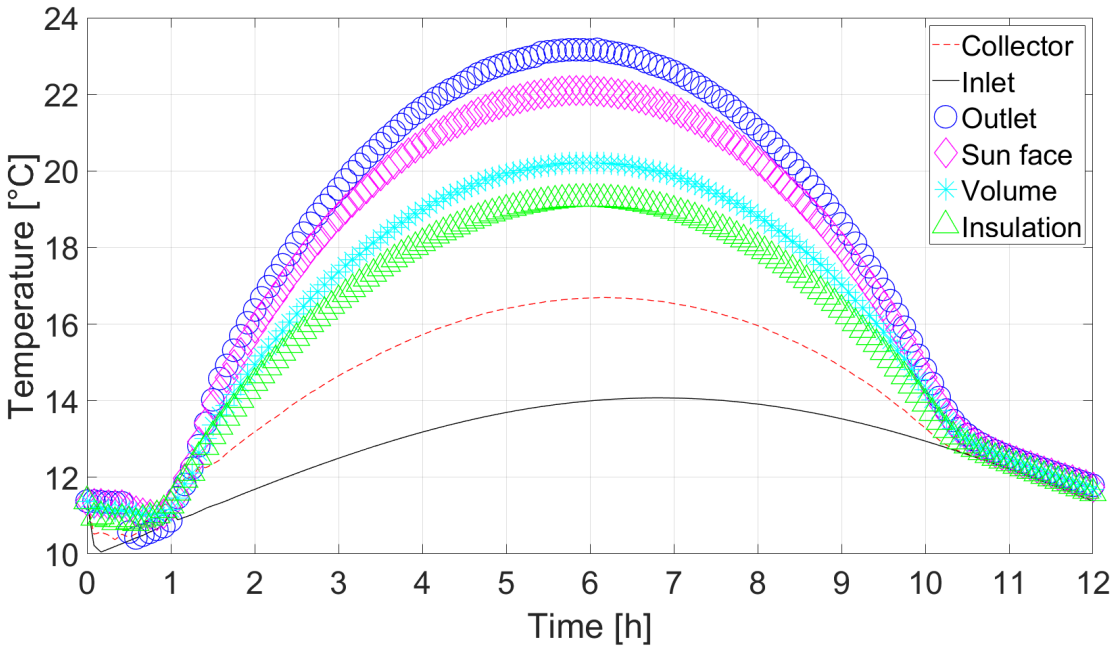

Figure 4.6: AEN12 average temperature.

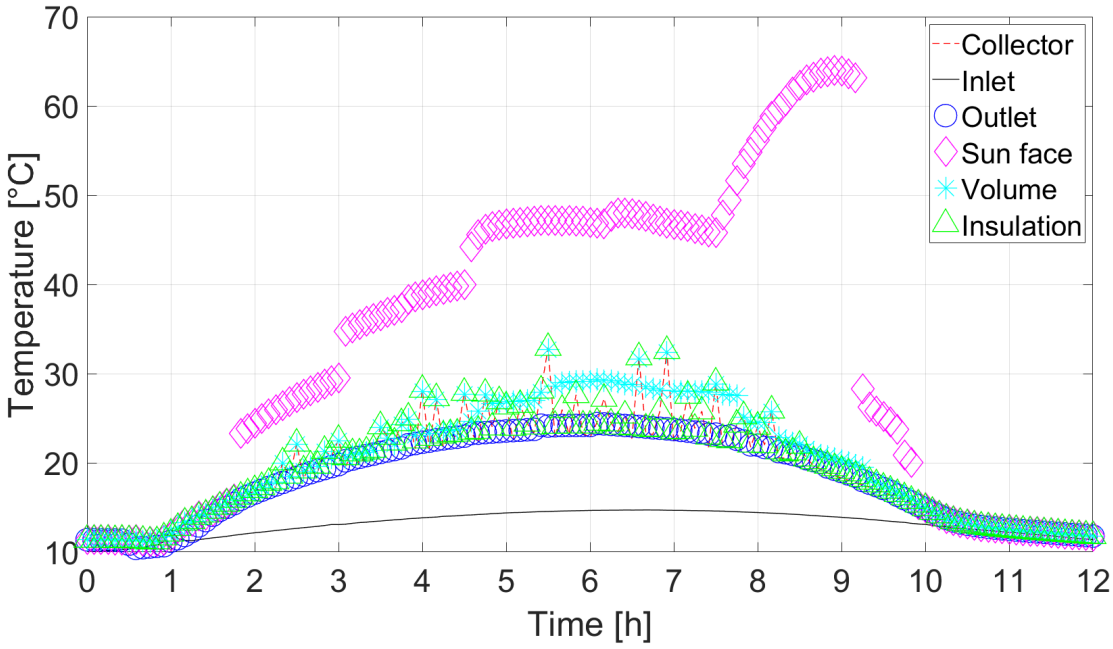

Figure 4.7: AEN12 maximum temperature.

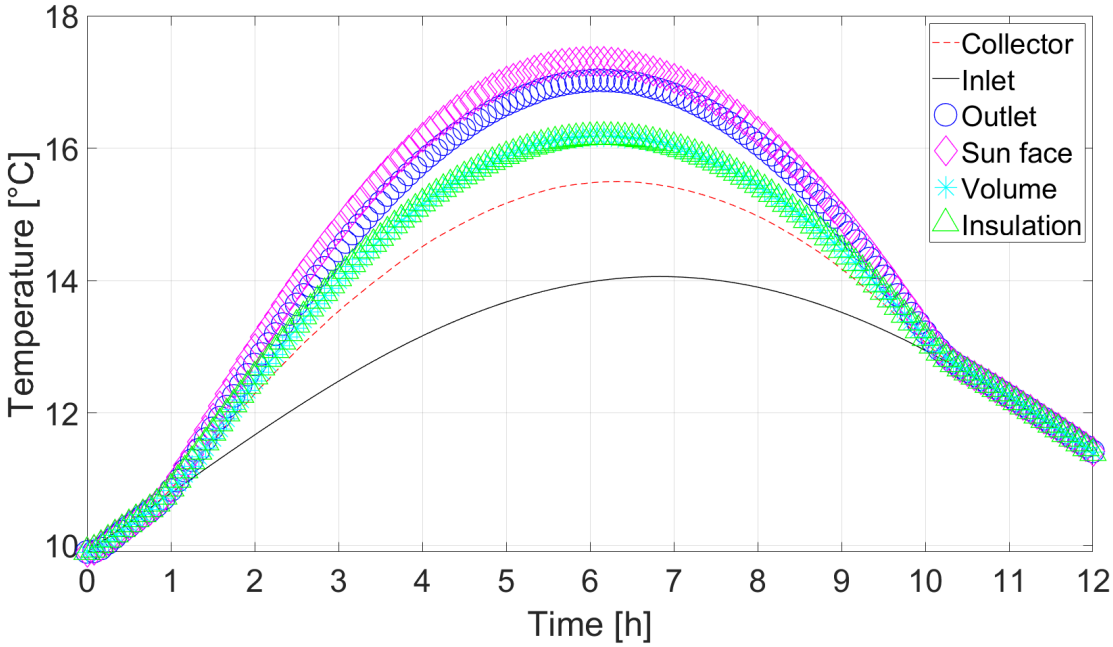

Figure 4.8: APF12 average temperature.

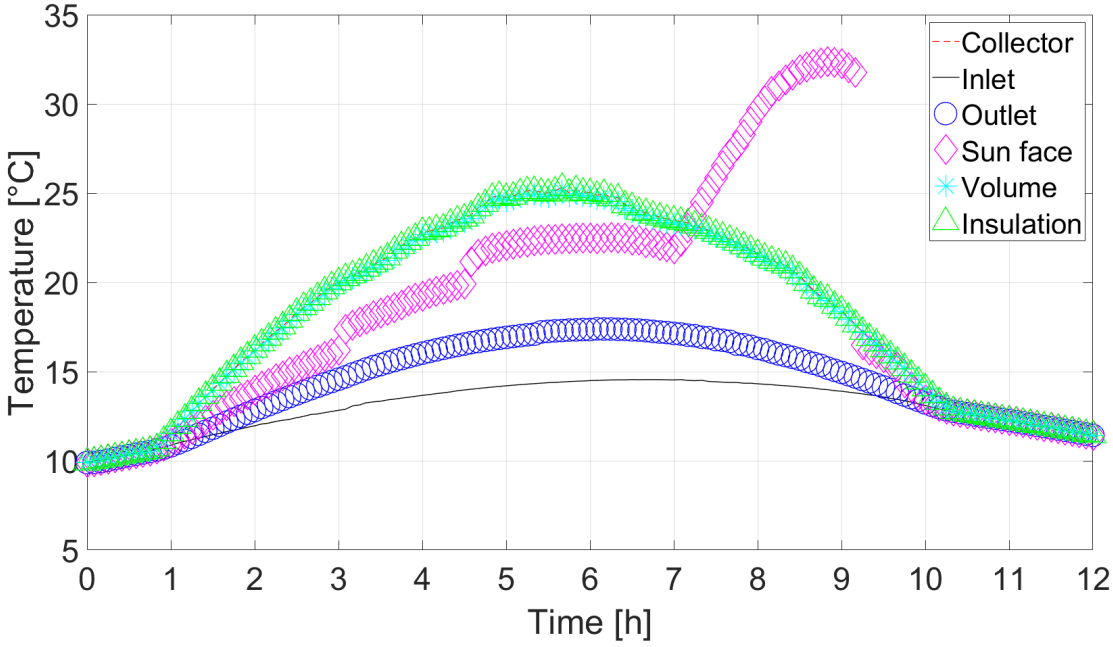

Figure 4.9: APF12 maximum temperature.

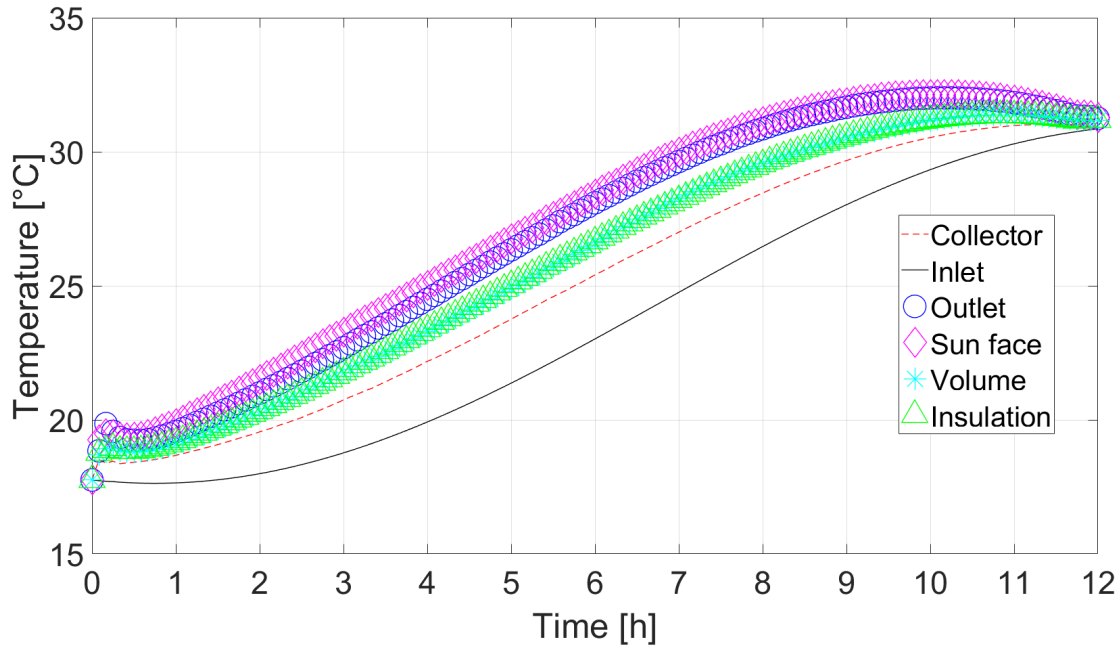

Figure 4.10: SPF12 average temperature.

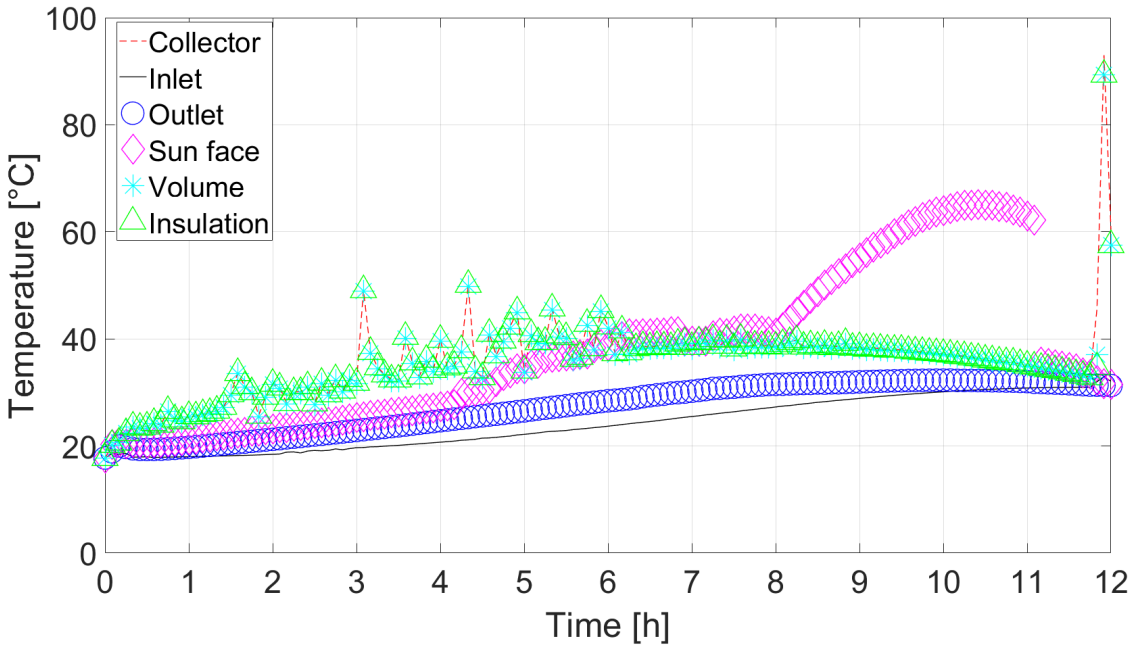

Figure 4.11: SPF12 maximum temperature.

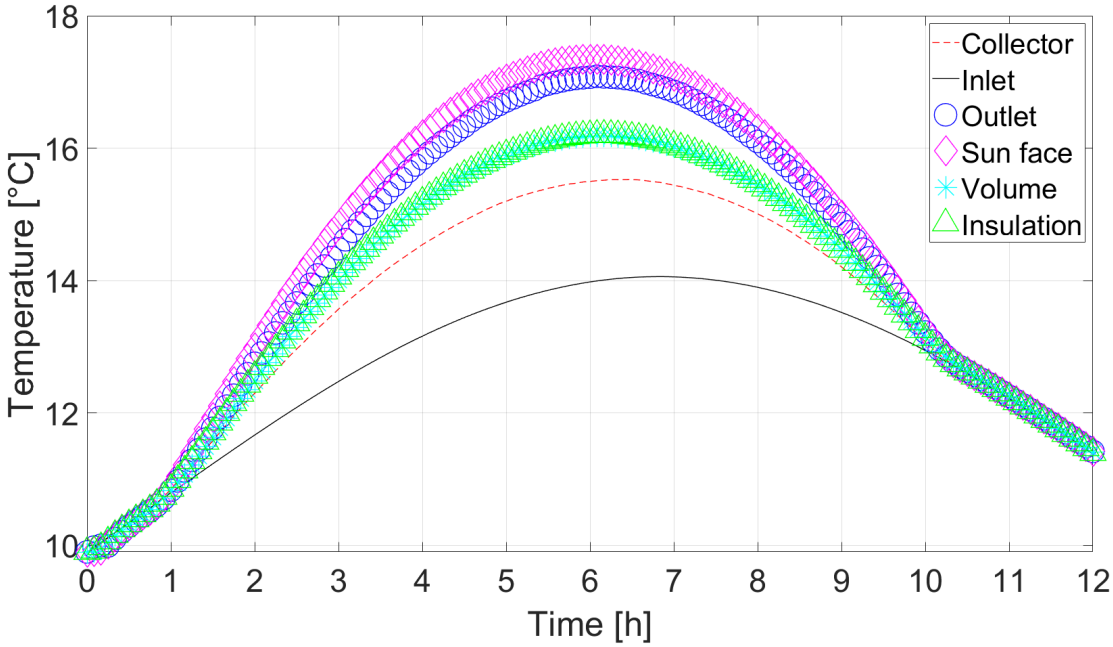

Figure 4.12: AEF12 average temperature.

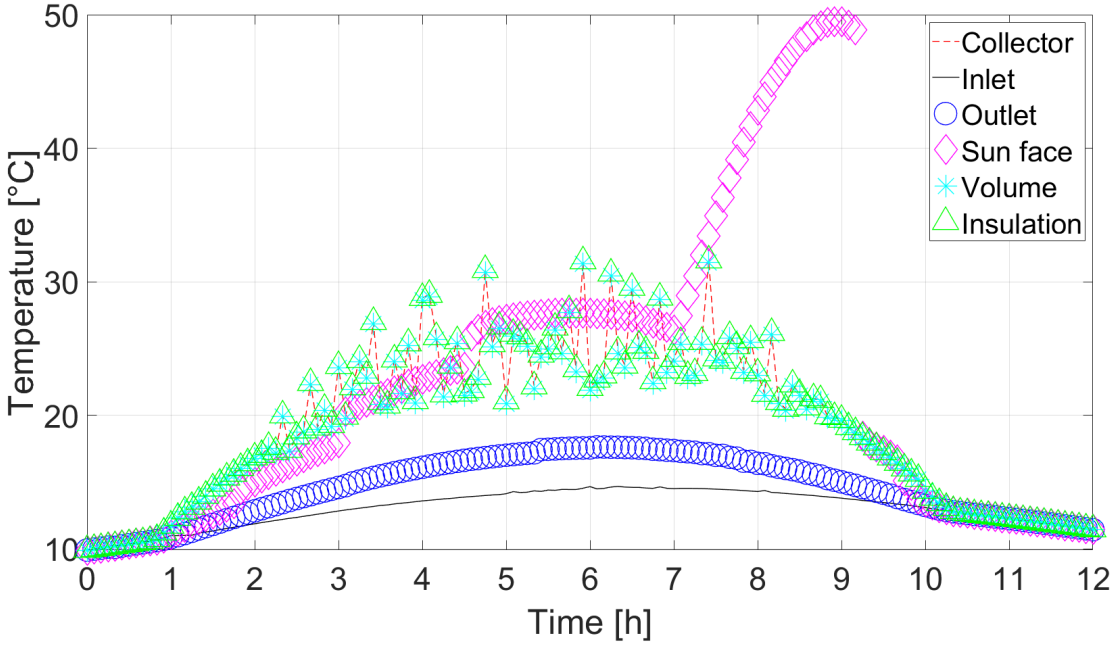

Figure 4.13: AEF12 maximum temperature.

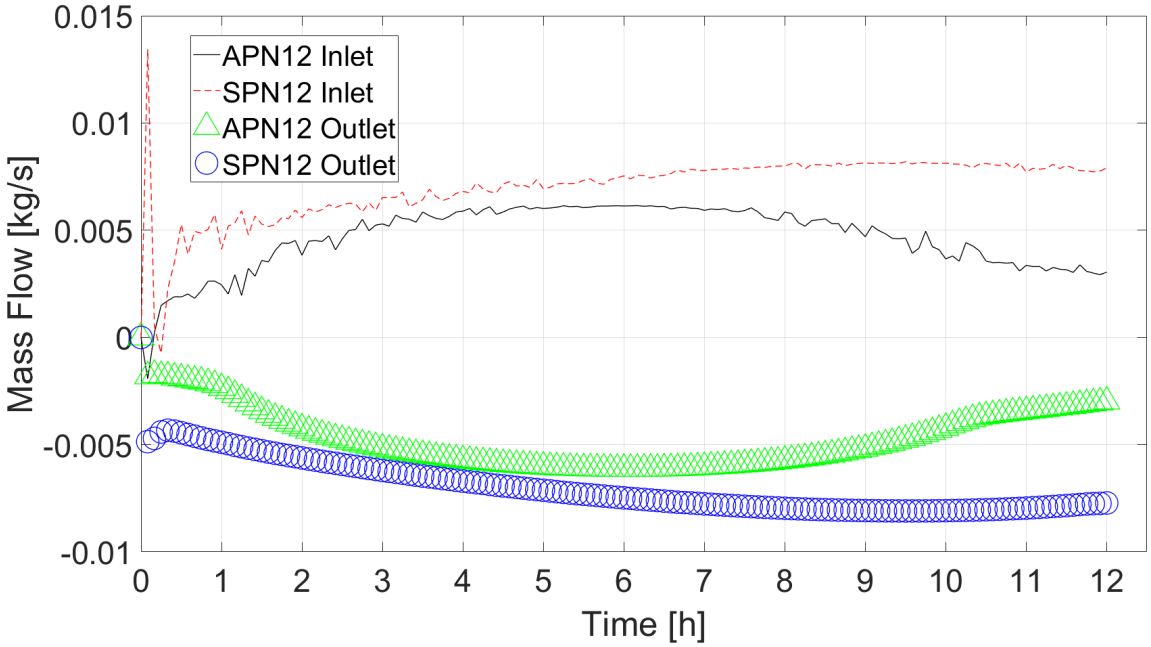

Figure 4.14: APN12 × SPN12 mass flow.

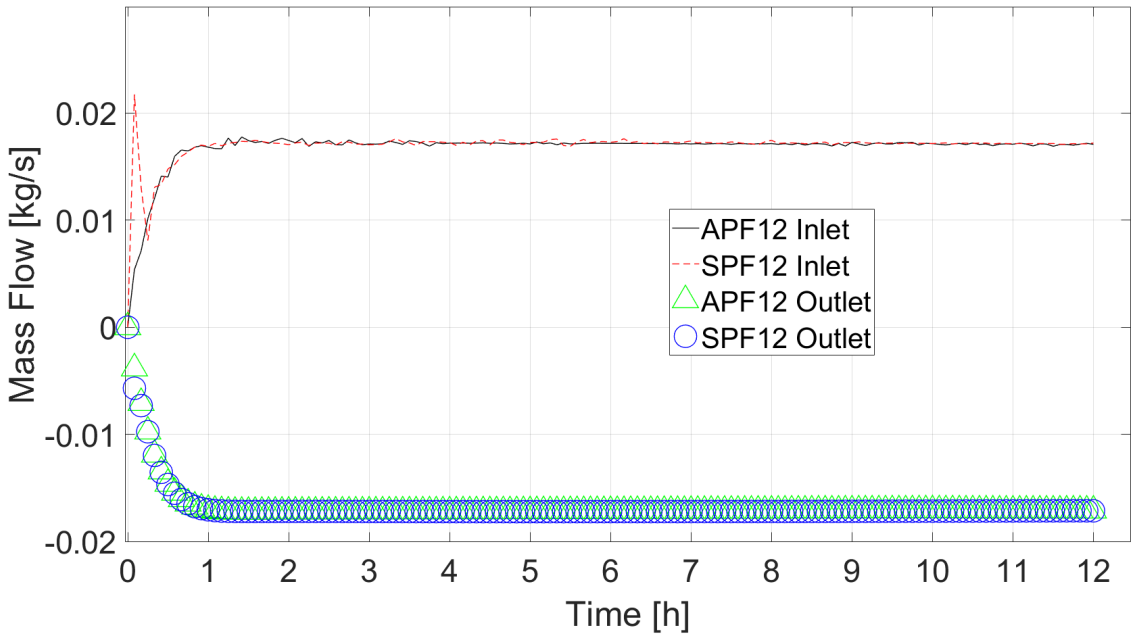

Figure 4.15: APF12 × SPF12 mass flow.

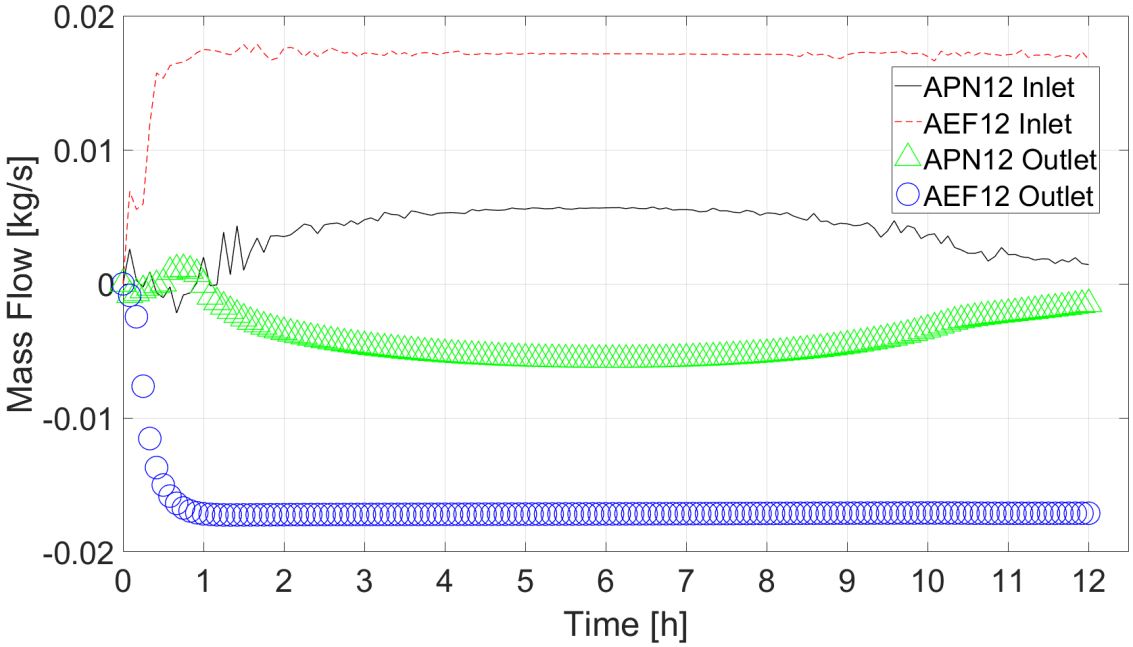

Figure 4.16: APN12 × AEF12 mass flow.

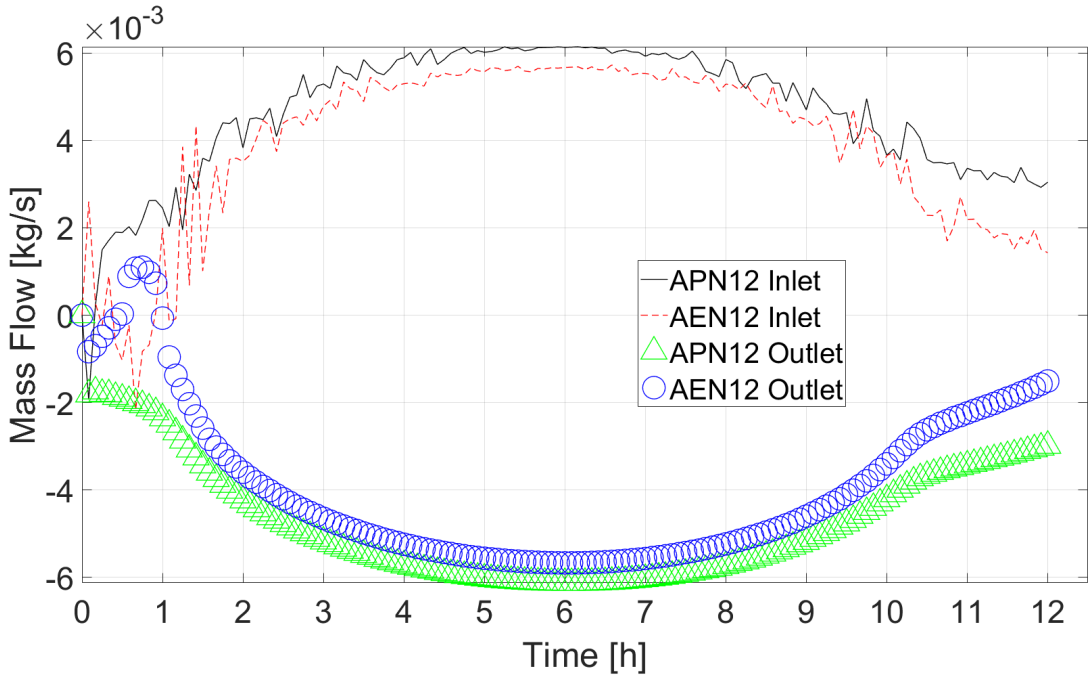

Figure 4.17: APN12 × AEN12 mass flow.

In Figures 4.18, 4.19 and 4.20, the black line continues to indicate **APN12**. The large dashed blue line indicates **AEF12**. The line of green circles, **SPN12**. The pink diamond line, **AEN12**. The yellow dotted line indicates **APF12**. The small red dashed line represents **SPF12**. The y-coordinate shows the exit velocity at the out face, at

the top of the chimney in $[m/s]$. On the x-coordinate is the simulated time in hours, starting before dawn.

Figure 4.18 shows the average outlet velocity of the six scenarios.

Figure 4.19 plots the cumulative integral of the Figure 4.18 values to obtain a mass delta at the end of the simulated time.

Finally, Figure 4.20 shows the average inlet velocity of the six simulations at the inlet vent of the collector.

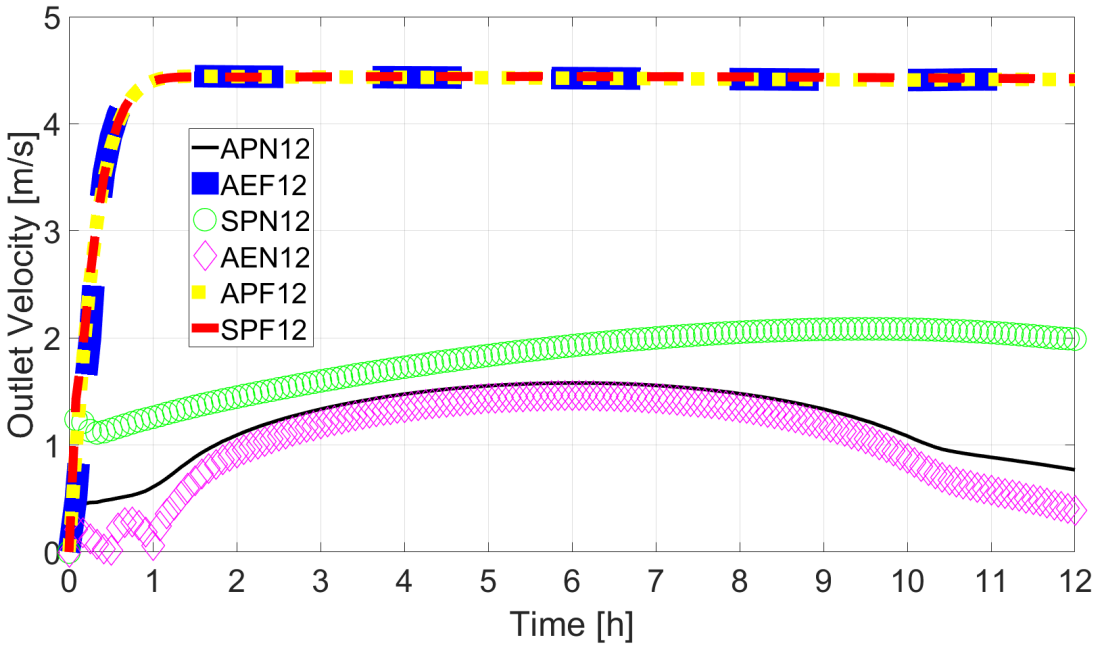

Figure 4.18: Outlet velocities.

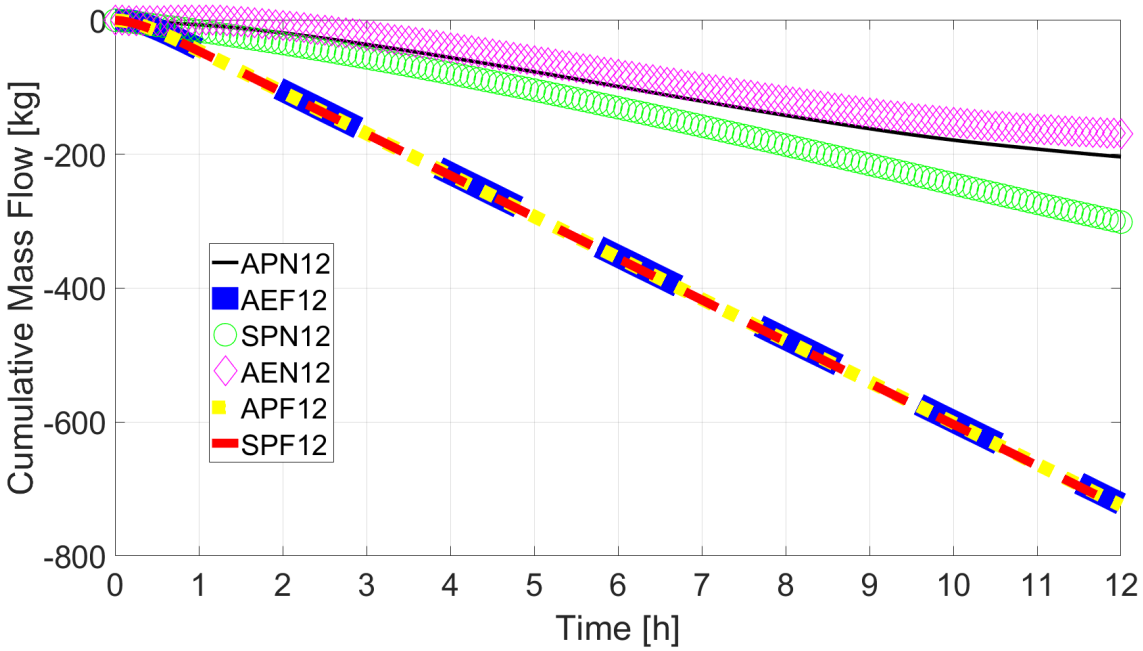

Figure 4.19: Outlet cumulative masses.

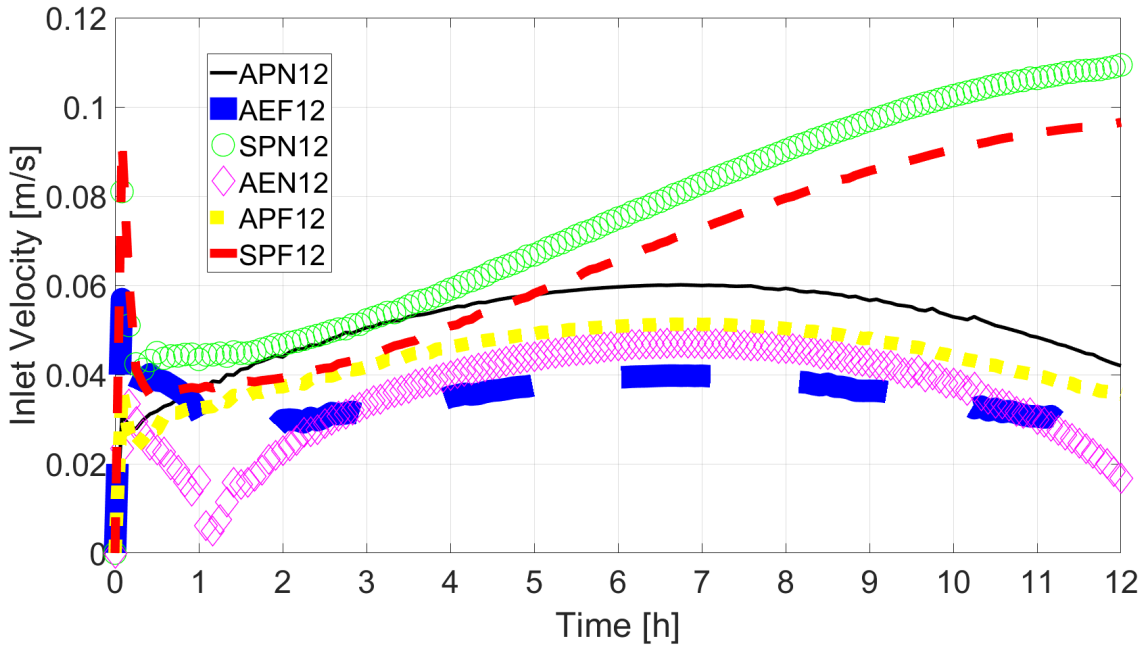

Figure 4.20: Inlet velocities.

Table 4.1 shows each mass delta from the Figure 4.19 simulations. The first three rows contain simulations of natural ventilation and the rest of forced ventilation.

Table 4.1: Delta Mass for 12 hours simulations.

Simulation	Delta mass $[kg]$
APN12	204
AEN12	169
SPN12	301
APF12	724
AEF12	722
SPF12	726

4.1.2 Simulated time of 20 hours

This section shows the 20-hour simulated time scenarios. Figures 4.21, 4.22, 4.23 and 4.24 follow the same legend as the average and maximum temperature figures above. Just as the y-coordinate shows temperatures in degrees celsius $[°C]$. The x-coordinate shows the simulated time in hours $[h]$, this time starting at 1 am.

It can be seen in advance that the variation between the active period, i.e. where there is radiation and the thermosiphon mechanism comes into play, is insignificant. As for the 12-hour simulations in summer, we have the temperature peak, thus the velocity peak.

The 20-hour simulations to assess the effectiveness of the equipment are unnecessary in the context of using computing time to generate data that will not be evaluated, data that is generated during the period without sunlight.

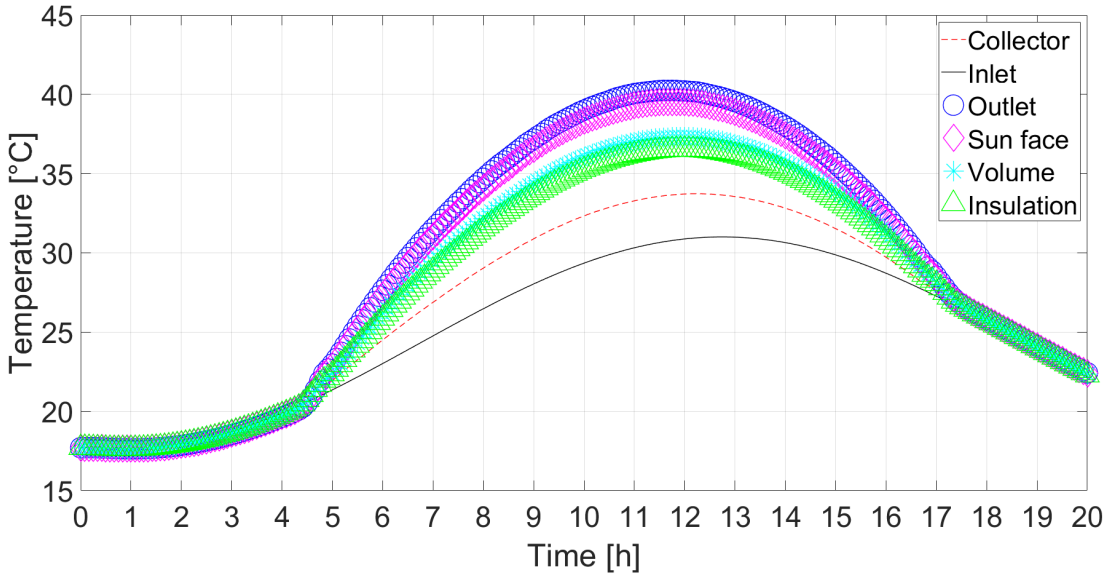

Figure 4.21: APN20 average temperature.

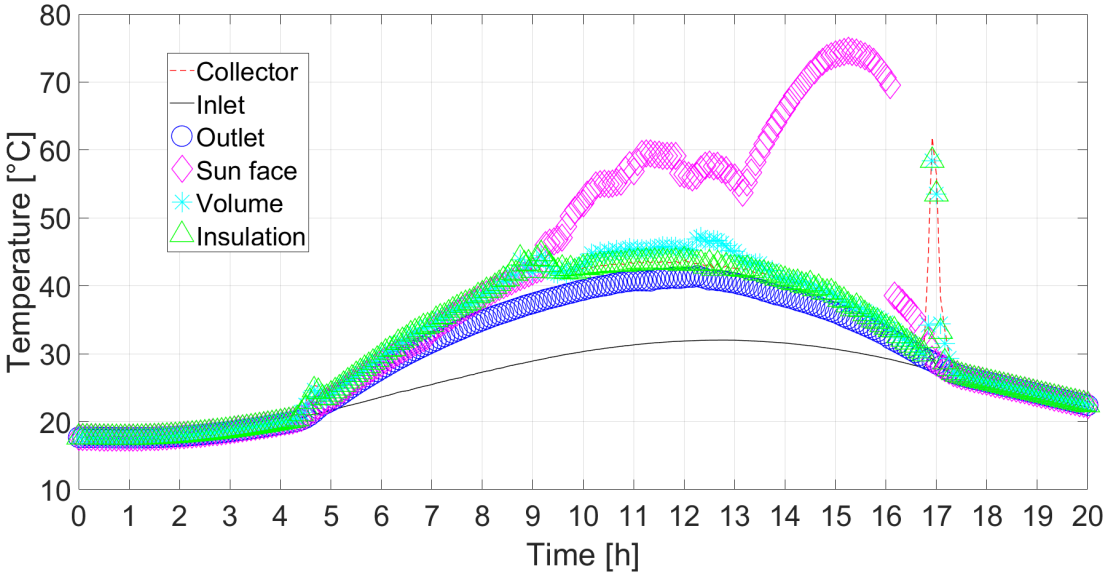

Figure 4.22: APN20 maximum temperature.

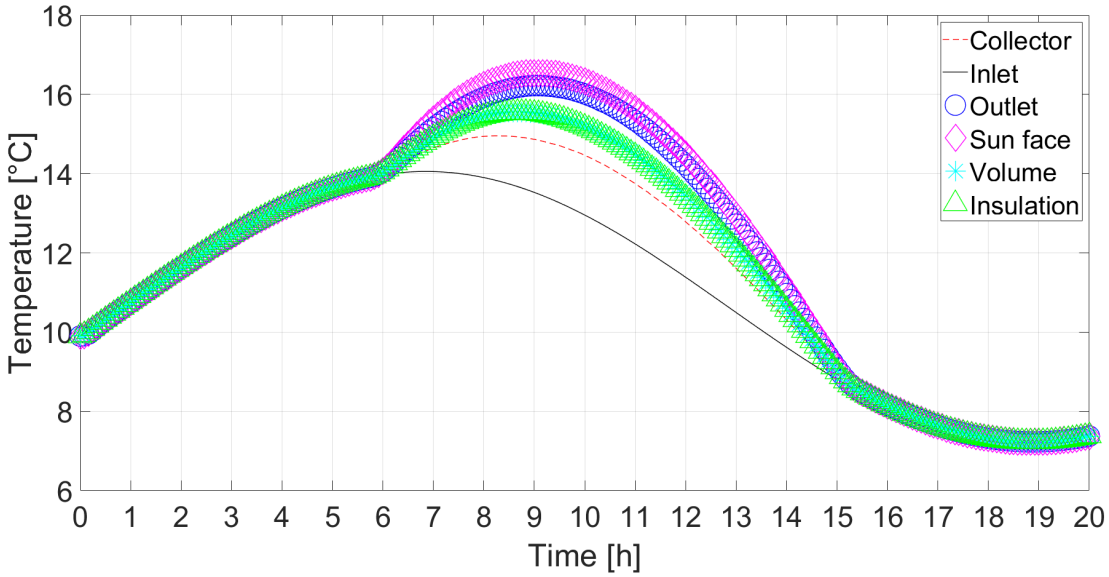

Figure 4.23: SPN20 average temperature.

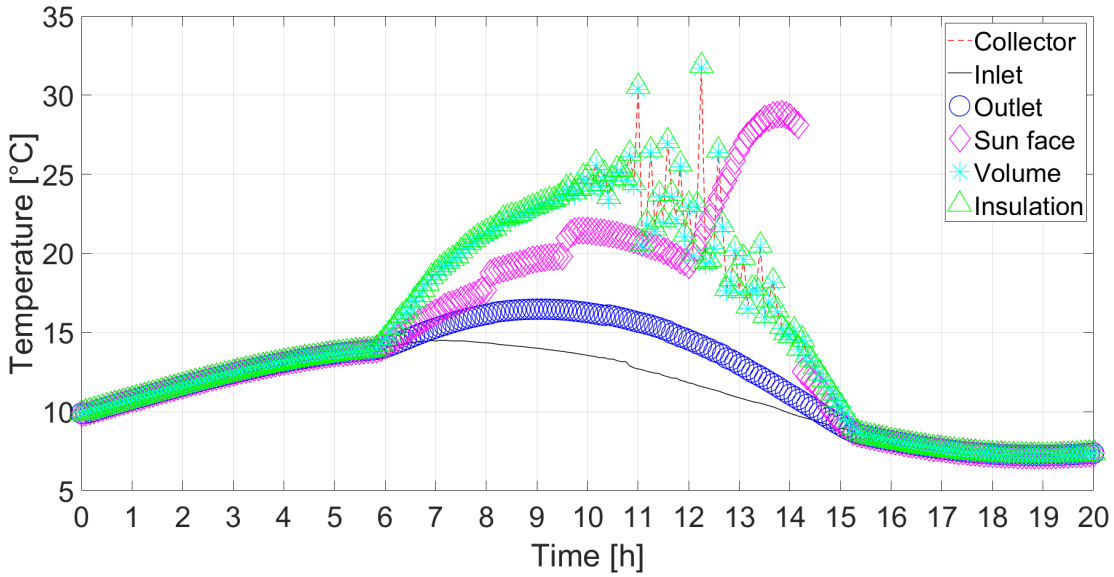

Figure 4.24: SPN20 maximum temperature.

4.1.3 Experimental data

Figure 4.25 shows a comparison of the experimental data with the maximum temperatures from **AEN12** simulation. Where the y-coordinate is the temperature in $[°C]$ and the x-coordinate is the time of day starting at midnight. Following the legend: **A** and **B** are the experimental data and **C** and **D** are the simulated data. The

data in **A** indicates the temperatures measured at the top of the chimney as illustrated in Figure 3.5a and the data in **B** of the middle sensor of the chamber present in the same figure. Line **C** indicates the temperature of the outlet face from the simulation in question and line **D** is the temperature of a point of the air volume matching the position from the middle sensor.

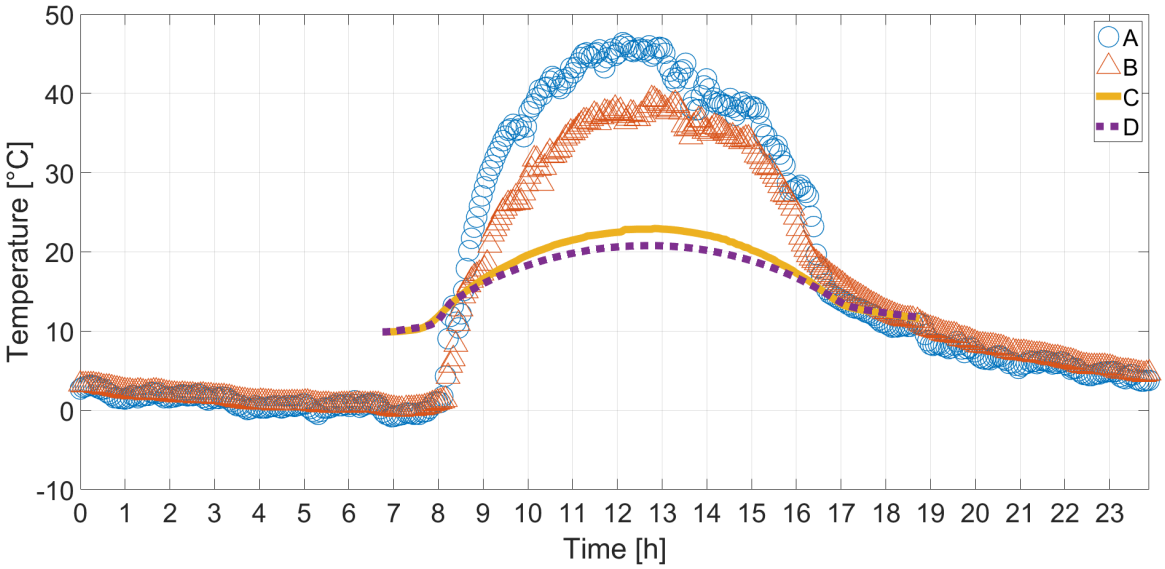

Figure 4.25: Experimental data × AEN12.

4.1.4 Temperature gradient

As observed in Figure 4.25, there is a temperature difference between the chimney and the chamber. This temperature gradient indicates that the thermosyphon is working. This gradient occurs at different heights inside the equipment, so it is possible to divide the temperature difference by the height difference, creating a $[\delta T/\delta z]$. This measurement shows the temperature difference per meter and will be used to evaluate the model.

In Figure 4.26 the x-coordinate shows the simulated $[\delta T/\delta z]$ and the y-coordinate the experimental one. The black dots are the data and the dashed red line divides the plot and is at 45°. The more the points coincide with the red line, the closer the model is to reality. Both figures compare the $[\delta T/\delta z]$ between the experimental and simulated. These plots were made by calculating the difference between the temperatures from the top of the chimney and the middle of the chamber and dividing this value by 3 meters, which is the height difference.

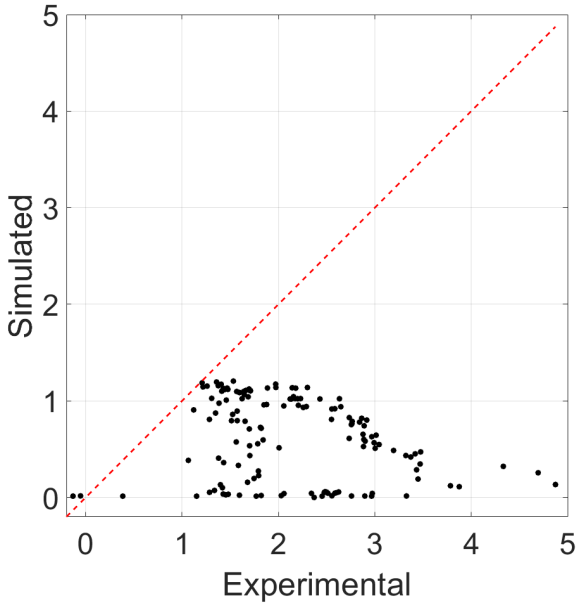

Figure 4.26: Experimental $[\delta T/\delta z]$ × AEN12 $[\delta T/\delta z]$.

4.2 Discussion

In this section, comparisons between the simulations will be made, comments on their behavior and explanations of the results. The effectiveness of the equipment will also be analyzed and suggestions for improving the design as well as the simulation process itself will be made.

4.2.1 Simulated time

Comparing the Section 4.1.1 and 4.1.2 figures, it can be seen that the period from dawn, is characterized by a big jump in temperatures, to the peak temperature on all faces appearing in all simulations. The objective is to study only the period when there are significant changes in temperature. For this reason and because of the comments in Section 4.1.2, only the 12-hour simulations will be discussed.

4.2.2 Singularity

In all the maximum temperature figures in all the simulations, there is a temperature peak just after the start of the second half of the simulation. The same peak is not observed in the experimental measurements and supposedly should not appear in the second half of the simulation, because from that moment on the radiation starts to decrease and the amount of energy read from the graph appears to be violating the first law of thermodynamics.

The first consideration is that all the graphs showing the maximum temperatures only show the temperature value of the hottest element on that face at that moment

in the simulation. This means that if one element is much hotter than all the others during the whole process, the interpretation of the results could be wrong. For this reason, it is necessary to look at the average and maximum temperature figures for the same simulation together.

The second consideration is the probable cause of this unexpected temperature spike. When simulating computationally using finite elements, the mesh directly influences the credibility of the simulation. In some cases, regardless of the size of the elements and their quantity, an event called a singularity can occur. The singularity in a finite element simulation is characterized when there is an edge or a sudden change in geometry, where the equation and the solution at that point will accumulate errors and may invalidate the simulation depending on how they occur. When observing the simulation results in Ansys Post, at the moment when the peaks occurred, it became apparent that they are generated by singularities.

Figure 4.27 shows the temperature contour of APN12. In the upper left corner, one can see the temperature scale that varies from 14.00 $^{\circ}C$ to 26.81 $^{\circ}C$. There are also three views in the same figure. On the left, a view chosen to better represent the context. The view in the upper right corner shows the internal part of the equipment as it faces the cutting plane. The view in the lower right corner shows the side that faces east, and shows the faces in contact with the environment. This figure represents the state of the simulation at timestep number 90, that is, 7.5 hours of simulated time, the same point where anomalies begin to be observed in the maximum temperature graphs.

At the moment represented by Figure 4.27, the expected temperature gradient is observed over almost the entire surface. There are colder regions in the collector region where the ambient air enters the system. Along its extension is heated by solar heat. Subsequently, the chamber and the chimney are at higher temperatures, therefore, in addition to being heated by the heat received from the sun it receives heated air from the collector. This temperature distribution is expected because due to the characteristic of natural convection.

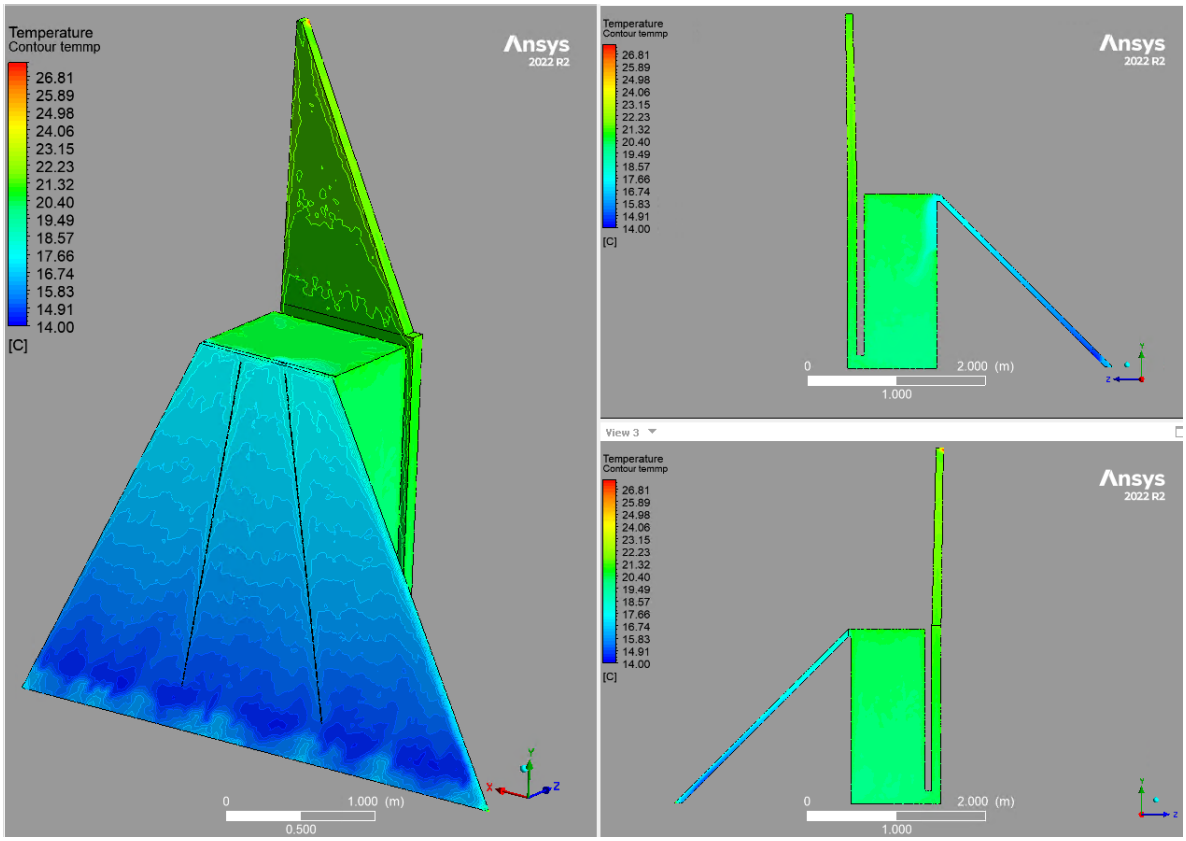

Figure 4.27: APN12 temperature contour timestep 90.

However, at this point in the APN12 simulation, two singularities could be observed. They are located at the end of the collector and at the top of the chimney. Figures 4.28 and 4.29 show the collector and chimney singularities, respectively. Both use the same structure as Figure 4.27 in relation to the views and the legend. They were zoomed in gradually to show how the surroundings of the singularity points have the expected temperature and only at the singularity point are there incongruities. It is possible to observe that near the points there is a gradient with higher temperatures and this is due to the thermal conduction of the material that, from the error point onwards, exchanges heat with the hottest element.

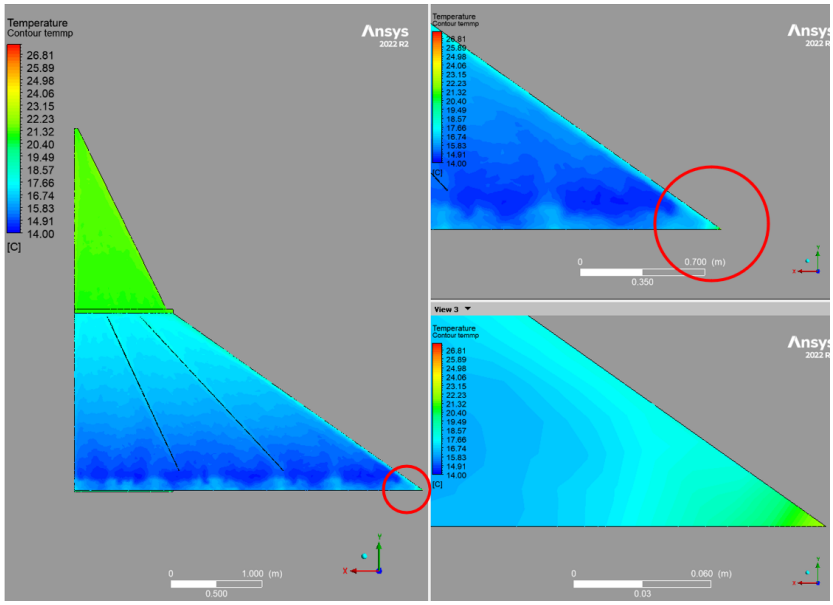

Figure 4.28: APN12 collector singularity.

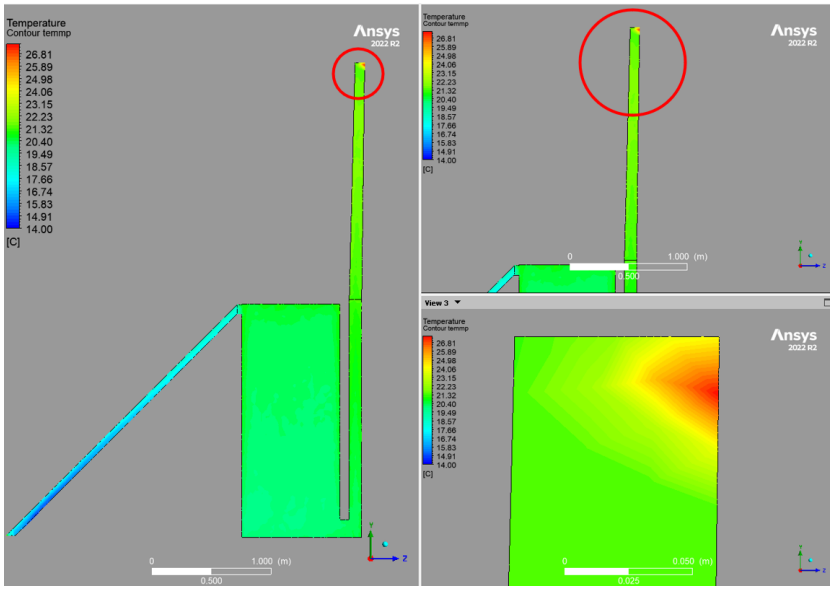

Figure 4.29: APN12 chimney singularity.

They occur at these specific points because the geometric conditions of these locations generate meshes with sharp edges or abrupt geometry breaks. Abrupt geometry breaks can be characterized by a right angle with few elements of the same size that do not allow a smooth transition. An example can be seen in Figure 4.30 which shows a print from the Fluent mesh editor at the end of the collector, also seen in Figure 4.28. In it, one can see how the mesh creates an edge to respect the geometry of the CAD design.

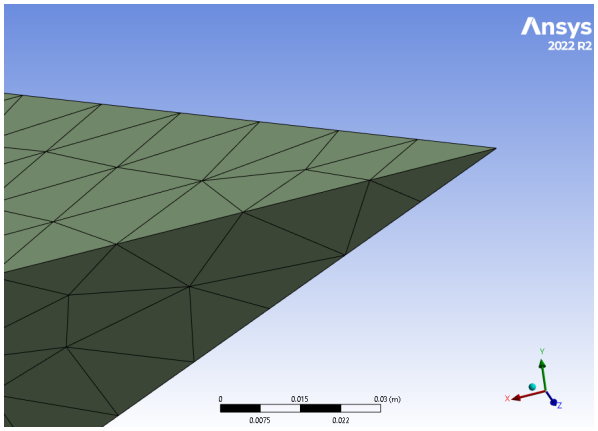

Figure 4.30: Collector's mesh edge.

This problem can be solved by changing the type of mesh construction or refining it, but the simplest way is to round the edges and corners directly in the geometry before creating the mesh. This solution was not applied in this work because there would not be time to redo the entire process.

Although the singularities cause these incongruities in the graphs, they do not invalidate the results. This can be seen by observing the average temperature graphs, which follow the predicted curve and, furthermore, the faces that should be hotter than the others due to the very nature of the process and the thermosiphon mechanisms are behaving as expected.

4.2.3 Temperature curves

In the average temperature curve graphs, the expected behavior was observed. This behavior is as follows.

The inlet temperature, represented by the solid black line, should be the lowest of all and also represents room temperature. This is because the inlet air temperature function follows the PVGIS database as seen in Figure 3.9 and due to the restrictions of the boundary conditions, this air is only heated when it enters the system, being heated by convection from the walls due to the radiation from the sun.

Next, the collector temperature, shown by the dashed red line, is the second lowest because it is there where the air will be heated, so the air upon entering passes through the collector and is gradually heated, at the same time that it gradually cools the collector, thus reducing its average temperature.

The next temperature on the scale is that of the air volume, represented by the cyan asterisks, and of the insulation, represented by the green triangles. They are equal most of the time because, as the insulation ends up not exchanging heat as efficiently as the rest, its temperature reaches equilibrium with the region in greatest contact, that is, the volume. However, since the insulation is an insulating material, some times the volume will rise more in temperature due to better thermal conductivity of the air.

The temperature of the Sun face, indicated by the pink diamonds, is in most cases the second highest. This also makes sense since it is the part that receives air and is heated in the same way as everything else. It can be surpassed in temperature by the Outlet, represented by blue circles, since the system outlet is precisely the Outlet and it is a system that is being heated, it is expected to be the hottest face. Sometimes the Sun face can surpass the Outlet, but it should be remembered that the Outlet itself is an opening, that is, the temperature measured there reflects the cutting plane of the volume of air that passes through there at that moment, that is, it is a reflection of the temperature of the volume and the Sun face. For this reason, they can coincide or vary little between each other.

In addition to this behavior being able to be analyzed in the average temperature figures, it can be seen in the temperature contour shown in Figure 4.31. In this figure there are two views that follow the same legend found in the scale in the upper left corner at $[°C]$.

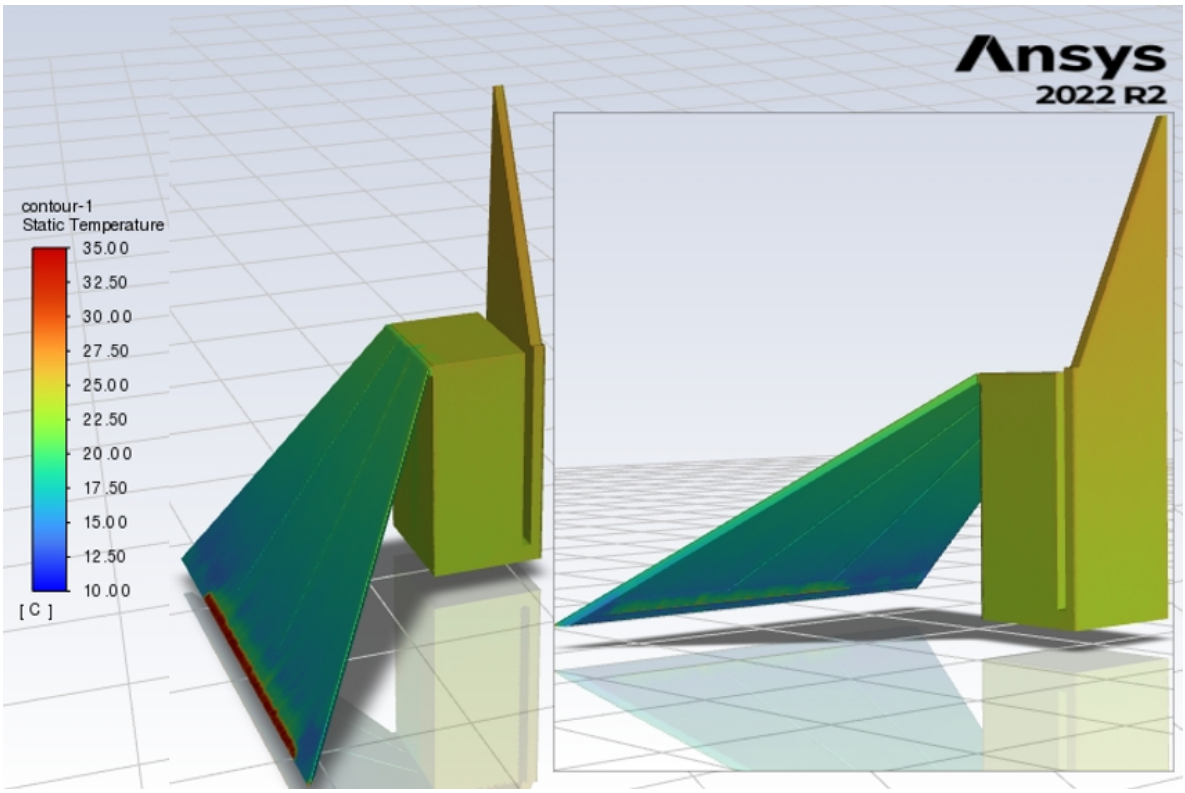

Figure 4.31: Temperature contours at six hours simulated.

In Figure 4.31 it can also be seen a high temperature zone at the bottom of the

collector. So far, you might think that there is a singularity, too. However, this event does not meet the requirements to be a singularity and occurs due to the characteristic geometry of the collector. In Figure 4.32 you can see an individual collector study. In this study, a simulation was performed just to check how the air travels through the geometry. This simulation has a forced ventilation input of 0.05 m/s and receives heat in the same way as all other simulations with respect to the autumn scenario. Where there are streamlines, it means that the air is moving, and where there are no streamlines it means stagnant air. This implies that at the base of the collector there is a pocket of air that does not move and, therefore, receives heat, increasing in temperature. This event generates the high temperature zone observed in Figure 4.31.

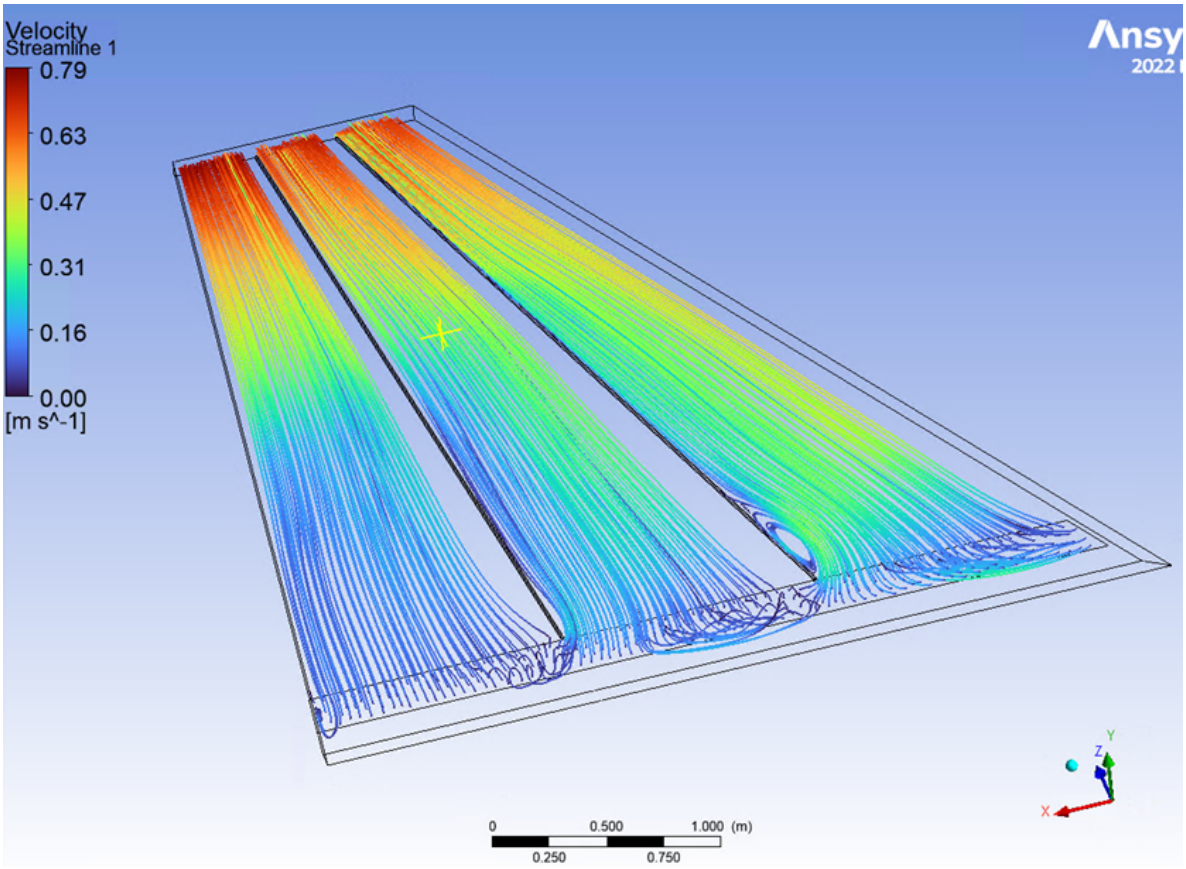

Figure 4.32: Streamline collector study.

Finally, one observed that the highest average temperature for the volume among all scenarios was 37.5 $°C$.

4.2.4 Flow curves

Looking at Figures 4.14, 4.15, 4.16 and 4.17 that are comparisons between the mass flows of some of the Section 4.1.1 simulations. The y-coordinate shows the mass flow in $[kg/s]$. The x-coordinate shows the time in hours following the same logic as the temperature plots.

Figure 4.14 makes a comparison between autumn and summer for the scenario with natural ventilation and radiation according to PVGIS. In the y-coordinate, positive values indicate mass entering the control volume and negative values mass leaving it.

It can be seen at the start of the process that the inlet lines show both positive and negative peaks. The negative peaks occur because at the start of the simulation, when there is still no radiation, the air is not heating up, the mass of air simply falls by gravity out of the volume since the inlet is an opening to the environment. The positive peaks at the beginning occur because the system is still stabilizing. It can be seen that the **SPN12** lines are more external than the **APN12** lines, indicating that they have a higher mass flow. This was to be expected since in summer there is more radiation and higher temperatures available for the process to take place more efficiently. Although this behavior is constant throughout the process, the difference in mass flow between autumn and summer is very low, with the biggest difference at the end of the process, $4.9 \times 10^{-3}\ kg/s$ for the inlet and $4.7 \times 10^{-3}\ kg/s$ for outlet, or respectively 1.59% and 1,58%.

It can also be seen that the plot is symmetrical, i.e. the mass entering the system is the same as the mass leaving the system, of course with small variations that are considered insignificant. From this plot, it can be said that higher inlet temperatures and more available radiation increase the performance of the equipment.

In Figure 4.15 at the beginning of the plot, we can see the system stabilizing. Then one can see that regardless of the time, the mass flows are the same in both simulations. This behavior was expected since the forced ventilation simulation scenarios emulate a fan with a constant flow rate. The graph is not continuous throughout because the pressure outlet boundary condition with target mass flow rate works in such a way that it varies the pressure as necessary to achieve the desired flow rate, in this case the one specified at Appendix A.

Compared to Figure 4.14, Figure 4.15 shows much higher flows at both stations with a maximum difference of $0.1 \times 10^{-3}\ kg/s$ after stabilization, or 0.00047%.

All the forced ventilation simulations show a flow rate varying between $17.11 \times 10^{-3}\ kg/s$ and $17.80 \times 10^{-3}\ kg/s$, which is expected given that the flow rate set in the boundary conditions was $17.15 \times 10^{-3}\ kg/s$. Figure 4.16 shows a comparison between the **APN12** and **AEF12** simulations. Even though the radiation data are not the same, the comparison is still valid, since, as will be explained later, radiation has little influence on the flow rate.

As can be seen in Figure 4.16, the most influential factor for performance is forced ventilation. The AEF12 simulation has a maximum flow rate of $6.14 \times 10^{-3}\ kg/s$ while the APN12 simulation has one of $17.15 \times 10^{-3}\ kg/s$. The differences in the inlet and outlet flow rates are $11.73 \times 10^{-3}\ kg/s$ and $11.11 \times 10^{-3}\ kg/s$, respectively, which means almost triple the mass flow rate.

In Figure 4.17 it can be seen that the mass fluxes of the simulations follow very similar behaviors, despite the radiation in **AEN12** being twice that of **APN12**. The maximum difference for inlet and outlet are respectively $0.41 \times 10^{-3}\ kg/s$ and $0.46 \times 10^{-3}\ kg/s$. This tiny difference indicates that radiation is not the greatest influence on the model.

Since radiation does not appear to affect the process, the question arises as to

whether the model itself works. In Figure 4.14 it can be seen that the summer scenario presents a slight improvement over the autumn one. This is due to differences in temperature. A greater temperature difference between parts of the equipment provides better flow in natural ventilation simulations. In Figure 4.2 it can be seen that when the x-coordinate is equal to 6 hours, the temperature difference between the ambient temperature, represented by the inlet and the volume, is 5.7 $°C$ and for the Sun face it is 7.5 $°C$. In Figure 4.4 the difference between the inlet and volume and the Sun face, at the same time, are, respectively, 7.9 $°C$ and 10.5 $°C$.

This greater temperature gradient is due to a combination of the greater amount of radiation and the higher initial air temperature in the summer scenario, since as there is more radiation, more energy will be supplied to the system and as the air is warmer it has more kinetic energy which favors heat exchange, allowing the heat received from radiation to be better used.

4.2.5 Cumulative mass

This section will cover Figures 4.18, 4.19 and 4.20.

In Figure 4.18, as expected, the simulations with forced ventilation have higher velocities, followed by the summer simulation with natural ventilation due to the effects of the higher temperature gradients.

Figure 4.19 compares the amount of mass that left the system, which is why the values are negative. As expected, the forced simulation cases present very similar values, being the largest in the comparison. Then comes the summer scenario with natural ventilation and then the other natural ventilation cases.

As observed in Table 4.1, even though the **AEN12** simulation had more radiation, the amount of mass at the end of the process was 18% smaller than **APN12**. This can be explained by variations in the simulation itself, through the cumulative error.

In Figure 4.20 it can be seen that the inlet velocities do not match all cases of forced ventilation as in the oultel plot. It can be seen that for the autumn cases the inlet velocities follow a similar behavior, while those in summer continue to rise until the end of the process. This phenomenon occurs because in addition to summer having greater temperature gradients, it also has more time of solar exposure. This indicates that the greater temperature gradient, causes greater velocities.

Based on this analysis, it can be seen that the best option for generating a higher flow rate is to implement forced ventilation.

4.2.6 Experimental $\times$ simulated data

In this section, Figures 4.25 and 4.26 will be discussed.

Since there were no measurements of the inlet or outlet speeds, it is impossible to know if the simulated velocities match the real ones. Load cell analyses, from the experimental testing, indicated a loss of 0.4 kg in 72 hours, this amount indicates stagnant air because constant airflow would take more mass as moisture out of the equipment.

As there is only data from one of the initially planned sensors, it is impossible to draw up a profile of experimental temperatures inside the chamber. Even if there are some construction problems, the conclusions drawn from the analysis of Figure 4.25, and Ansys reports indicate that the simulation procedure is correct but with low precision.

The measured temperature values are around 20 $°C$ higher than the simulated ones. The difference should not be that great, since in a simulated scenario, which does not lose heat to the external environment, one would expect that the simulated temperatures would be higher than the measured ones.

The higher temperatures in the experimental data may be the result of several factors:

1. The inlet temperatures used in the simulation may differ from the actual temperature on the test day in question. Since there are no temperature sensors on the outside of the equipment the temperature from PVGIS had to be used;

2. Due to a failure in the supplier's technical capacity to follow the project as initially designed, there is a possibility that the collector is not working the whole time, that is, the internal air may be heating up more than expected because it is stagnant. The most probable cause is the tarp malleability, when the wind strikes the collector it may deform it, even blocking airflow inwards. This behavior is also possible for the chimney and chamber;

3. It may be that on the date in question conditions varied from the databases used enough to generate the differences observed in the plot, even if unlikely;

4. The model may be inaccurate and need to be refined. Using smaller elements and a smaller time step value;

5. Any combination in any proportion of the items above.

In Figure 4.26 the measured data ranges from $-0.53\ °C/m$ to $4.87\ °C/m$, with an average of $1.94\ °C/m$. Simulation data ranges from $0.01\ °C/m$ to $1.20°C/m$ with an average of $0.58\ °C/m$. The difference between these $[\delta T/\delta z]$ is expected once Figure 4.25 presents higher experimental temperature values.

At Figure 4.26 at the x-coordinate 80% of the values are between $1.2\ °C/m$ and $3.5\ °C/m$. At the y-coordinate, around 50% of the values are above $0.5\ °C/m$ while the other half are below. When the averages of the two sets are compared, the measured values are 3.34 times higher. The closer to the central line the black dots are the better the model represents reality.

The fact that the experimental temperature values are bigger, i.e. are below the dashed line, indicates stagnant air, as mentioned before. As for why the air is stagnant there are two possible reasons.

The first is a cyclical behavior that arises in the operation of the equipment. The higher the $[\delta T/\delta z]$, the higher the speed due to the thermosiphon phenomenon. However, the higher the velocity, the lower the air temperature because it has less time to exchange heat with the walls. This would result in intermittent operation: the air is heated and gains speed and this hot air escapes to the outside and gives way to cold

air, which has less speed and needs to be heated to start the cycle all over again. This scenario becomes unlikely if the malleability of the tarpaulin material, that involves the structure is a major interference.

The second is if external factors prevent the equipment from working and the air therefore gets too hot. For example, if the malleability of the canvas makes it possible for the wind to force one wall against the other, blocking the air inlet or outlet, the interrupted flow would cause the air to heat up for longer.

As the simulated control volume does not take into account the malleability of the tarpaulin, being 100% rigid, it is possible that the excessive heating is due to those external interferences. On the other hand, temperature differences as large as 20 $°C$ question the accuracy of the model. This is because as there are no temperature losses to the environment, one would expect a temperature range closer to the measured one, even if the $[\delta T/\delta z]$ remained close to the average of 0.58 $°C/m$.

4.2.7 Ventilation

The purpose of this section is to discuss the effectiveness of the equipment, regarding natural and forced ventilation.

The internal velocities and the total amount of mass leaving the system at the end of a cycle are very different between the forced and natural ventilation scenarios. Although it is necessary to refine the model, and with this refinement there may be an improvement in these values, according to the literature, natural convection alone has a limitation on the velocities it can generate.

Looking at Table 4.1 one can see that in the autumn simulations, the amount of mass leaving the system is 3.8 times greater for the forced ventilation scenario and 2.4 times greater for the summer simulations. As this is a dehydrator that needs to expel moisture through an air outlet, the higher the mass flow rate throughout the process, the more effective the equipment will be.

This difference in mass flow indicates that forced ventilation is necessary. Even if the model needs to be improved to measure the temperature and $[\delta T/\delta z]$ values, installing a fan in the chimney would ensure air circulation in adverse conditions. For example, on cloudy days and at night, even if the temperature drops is most desired to have a guaranteed air flow with low temperatures than technically no air flow. Finally, the cost of the fan, panel and battery would not make the equipment more expensive and the benefits of this measure would be worth the investment.

One can observe the advantage of forced ventilation by analyzing Figure 4.33, where there are two volume renderings of the internal air velocity, with the scales in $[m/s]$ ranging from zero to 1.00 m/s, the render on the left represents **APN12** and the one on the right **APF12**, at the same instant represented by six hours of simulated time, that is, the peak velocity. It is possible to clearly see that in the case of **APF12** there is in fact an air flow that goes from the inlet to the outlet. While in **APN12** the transparency within the volume represents stagnant air, that is, the non-functioning of the thermosiphon.

The internal velocities for the case of forced ventilation are in the order of 0.25 m/s, while with natural ventilation they are virtually zero. This behavior is similar in all

simulations, that is, natural ventilation does not generate satisfactory internal flow and forced ventilation creates desired flow.

In addition, as there is more mass flow with fans, the average temperatures are lower. Drying at lower temperatures may be more desirable because there is less risk of damaging the organoleptic properties of the food, due to the deterioration of the proteins as a result of the high temperature.

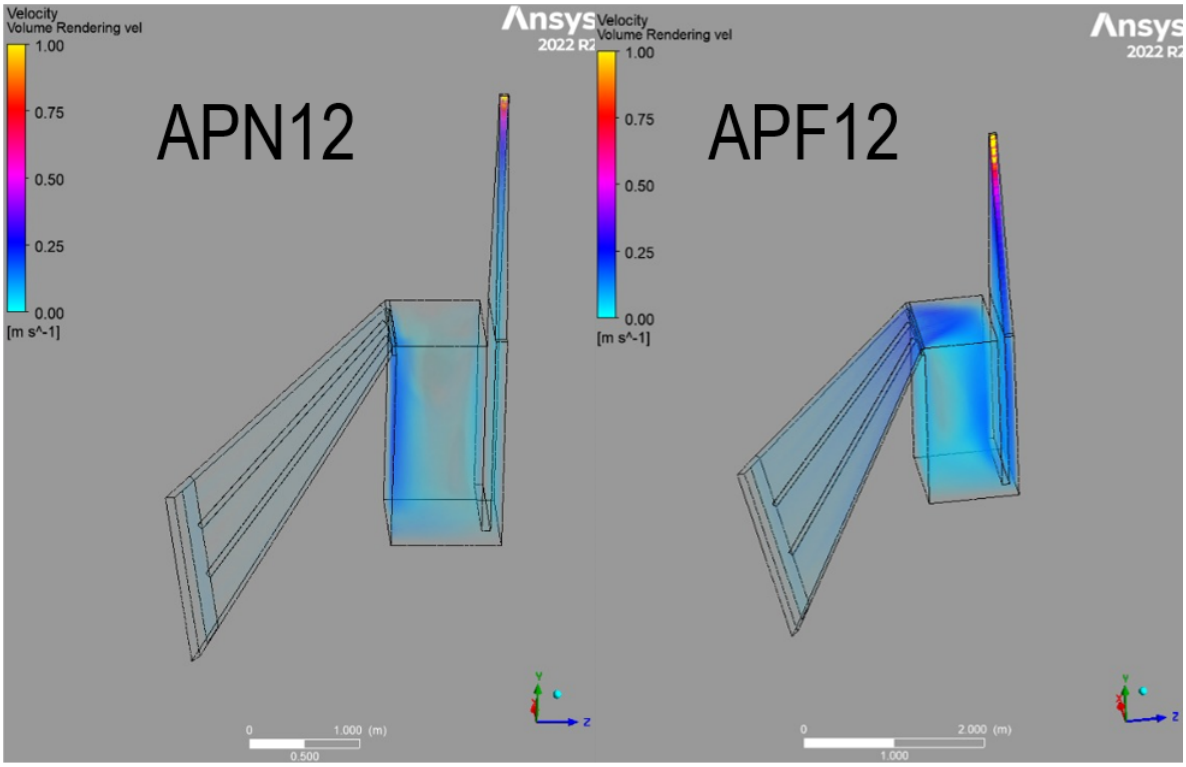

Figure 4.33: Internal velocities comparison.

Chapter 5

Conclusion

The objective of this work was to model the dehydration in a MSD and to perform CFD simulations to analyze the behavior of this equipment in different scenarios to compare them to experimental data. The prototype was tested at the end of 2023 and the data from that work generated three publications.

The simulation process was built using the Ansys 2023 R2 software, using the Ansys Fluent subprogram. Data processing was done with Matlab software. To reach the final process, more than one hundred simulations were performed, accumulating approximately 400 hours of computational time.

Heat loss due to mass loss from the dehydration of the acorns was not considered. This was not done due to insufficient time to study the diffusivity process and how to implement it computationally.

The simulation configuration and parameters were described and justified in detail. Among these choices, it was described which data would be acquired from the simulations through the report definitions tool. The data collected for all faces and for the air volume includes average and maximum temperatures [$°C$], average mass flow [kg/s], and average speed [m/s].

For the purpose of data analysis, six final simulations were performed. These analyses evaluate the scenarios, differentiating them between the summer and autumn seasons, between radiation measured in the tests and the PVGIS database, between having or not having forced ventilation, and between simulated times of 12 and 20 hours. An alphanumeric classification system was created to differentiate the simulations from each other.

From these simulations, graphs were presented with the average and maximum temperatures of each scenario. The temperature plots behaved as expected if the model was correct as expected. These plots indicated a maximum average air temperature of 37.5 $°C$, which is in the safe range for preserving the nutrients.

Additionally seven plots comparing the flows of the simulations were also presented to explain how the variables influenced the results. In the case of natural ventilation, the summer scenarios show respectively 1.59% and 1.58% higher inflow and outflow rates. In the case of forced simulation, the difference is 0.00047% since the flow rate is forced to be the same. The forced ventilation scenarios have an inlet and outlet flow rate that is three times higher.

Plots of the total mass leaving the system were also made to assess the need for forced ventilation. Coming to the conclusion that forced ventilation is about three times better than natural ventilation and is needed to ensure a continuous operation at night and in low radiation situations.

In the maximum temperature curves, a temperature peak was observed that appears

to violate the first law of thermodynamics. This event occurred due to a singularity in the simulation, due to geometric parameters, and it was concluded that this would not influence the results.

The databases used and the experimental data showed great divergence in values. Correction factors were used to address this divergence.

The simulated data were then compared to the experimental data. It was observed that the model is a lot different from the measured results. Hypotheses were put forward that point to causes both in the construction of the equipment and in the model itself. As explained, the most likely cause is the model's lack of precision. This is why it needs to be improved.

For future work the following is suggested:

1. Review the databases and cross-reference them with other different databases to check whether discrepancies between experimental and simulated data are due to a failure in the database or field measurements;

2. Combine the simulation process created with mass transfer and its heat loss, in order to simulate moisture loss by diffusivity;

3. Create design changes to study how to improve airflow by changing both the collector, chamber and chimney;

4. For future experimental tests, implement air speed sensors at the inlet, outlet and inside the system, in addition to improving the thermal sensor web;

5. Improve the model by refining the mesh and reducing the size of the calculation time step. Although this has a higher computational cost, the accuracy gained will help to better predict real situations.

Bibliography

[1] Bernardo Farrero, Paulo Bruno Rossi da Silva, and Luis Frölén Ribeiro. Revisiting solar dryers for small to medium production. In Jorge Filipe Leal Costa Semião, Nelson Manuel Santos Sousa, Rui Mariano Sousa da Cruz, and Gonçalo Nuno Delgado Prates, editors, *INCREaSE 2023*, pages 347–362, Cham, 2023. Springer Nature Switzerland.

[2] Paulo Bruno Rossi da Silva, Bernardo Farrero, and Luis. Frölén Ribeiro. A novel design approach for solar dehydrators. *Consolfood*, 2023.

[3] Paulo Bruno Rossi da Silva, Bernardo Farrero, Arthur Marangoanha Silva, Pedro Babo, and Luis Frölén Ribeiro. Responsive dehydration: Sensor-driven optimisation of production cycles in a solar dehydrator. In *SMARTINDUSTRY-2024: International Conference on Smart Automation & Robotics for Future Industry*, Lviv, Ukraine, April 18–20 2024. CEUR Workshop Proceedings. Published under Creative Commons License Attribution 4.0 International (CC BY 4.0).

[4] Food and Agriculture Organization Of United Nations. Frutas y verduras – esenciales en tu dieta. año internacional de las frutas y verduras, 2021. documento de antecedentes. `https://doi.org/10.4060/cb2395es`, 2020. Accessed in data 10/03/2023.

[5] Romeo T. Toledo, Rakesh K. Singh, and Fanbin Kong. *Fundamentals of Food Process Engineering*. Food Science Text Series. Springer Cham, 4 edition, 2018. Published: 09 October 2018, Hardcover: Published 20 October 2018, Softcover: Published 03 January 2019.

[6] Instituto Nacional de Tecnología Agropecuaria. Instituto nacional de tecnología agropecuaria. `https://www.argentina.gob.ar/inta`. Accessed in data 10 March 2023.

[7] A. Mujumdar. Drying technology - an overview, 2011. Notes of Industrial Transfer Processes, National University of Singapore.

[8] Yunus A. Çengel and Afshin J. Ghajar. *Heat and Mass Transfer: Fundamentals and Applications*. McGraw-Hill Education, 5th edition, 2015. SI Edition.

[9] Frank P. Incropera, David P. DeWitt, Theodore L. Bergman, and Adrienne S. Lavine. *Fundamentals of Heat and Mass Transfer*. John Wiley & Sons, Hoboken, NJ, USA, 6th edition, 2007.

[10] Sadik Kakaç and Altuğ Yüksel. *Handbook of Single-Phase Convective Heat Transfer*. Wiley-Interscience, 1985.

[11] Adrian Bejan. *Convection Heat Transfer*. John Wiley & Sons, 4 edition, 2013.

[12] William A. Beckman John A. Duffie. *Solar Engineering of Thermal Processes*. John Wiley Sons, Ltd, 2006.

[13] S. C. Chapra and R. P. Canale. *Numerical Methods for Engineers*. McGraw-Hill Education, New York, 7th edition, 2015.

[14] O.C. Zienkiewicz, R.L. Taylor, and P. Nithiarasu. *The Finite Element Method for Fluid Dynamics*. Elsevier, 6th edition, 2005.

[15] J.N. Reddy. *An Introduction to the Finite Element Method*. McGraw-Hill, 2nd edition, 1993.

[16] J. Donea and A. Huerta. *Finite Element Methods for Flow Problems*. John Wiley & Sons, 2003.

[17] T.J.R. Hughes. *The Finite Element Method: Linear Static and Dynamic Finite Element Analysis*. Dover Publications, 2012.

[18] H. K. Versteeg and W. Malalasekera. *An Introduction to Computational Fluid Dynamics: The Finite Volume Method*. Pearson Education Ltd., Harlow, England, 2nd edition, 2007.

[19] Poonam Rani and P.P. Tripathy. Cfd coupled heat and mass transfer simulation of pineapple drying process using mixed-mode solar dryers integrated with flat plate and finned collector. *Renewable Energy*, 217:119210, 2023.

[20] Deisy Becerra, Alexander Zambrano, Miguel Asuaje, and Nicolas Ratkovich. Experimental and cfd modeling of a progressive cavity pump (pcp) using overset unstructured mesh part 1: Single-phase flow. *Geoenergy Science and Engineering*, 234:212602, 2024.

[21] Clement A. Komolafe, John O. Ojediran, Faith O. Ajao, Oluwasogo A. Dada, Yemisi T. Afolabi, Iyiola O. Oluwaleye, and Adewumi S. Alake. Modelling of moisture diffusivity during solar drying of locust beans with thermal storage material under forced and natural convection mode. *Case Studies in Thermal Engineering*, 15:100542, 2019.

[22] A.H Bahnasawy and M.E Shenana. A mathematical model of direct sun and solar drying of some fermented dairy products (kishk). *Journal of Food Engineering*, 61(3):309–319, 2004.

[23] Marcia Mantelli. *Thermosyphons and Heat Pipes: Theory and Applications*. 01 2021.

[24] European Commission. Pvgis plataform. `https://re.jrc.ec.europa.eu/pvg_tools/en/#MR`, 2024. Accessed: 25 June 2024.

[25] The Time Now. The time now. `https://www.thetimenow.com/img/coordinated_universal_time`, 2024. Accessed: 25 June 2024.

[26] G. K. Batchelor. *An Introduction to Fluid Dynamics*. Cambridge Mathematical Library. Cambridge University Press, 2000.

[27] Goodfellow. Additive free polymer ldpe coil. Technical report, Goodfellow Advanced Materials, 2024.

[28] Brasken. Boletim técnico n°03 pvc: Propriedades de referência dos compostos de pvc. Technical Report 3, Brasken, 2002.

[29] *Ansys Fluent Workbench Tutorial Guide*, 2024.

This page has been intentionally left blank.

Appendix A

Manufacturer's catalog

Additional Resources: Product Page

CUI DEVICES

date 10/15/2021
page 1 of 7

SERIES: CFM-80BG | **DESCRIPTION:** DC AXIAL FAN

FEATURES
- dual ball bearing system
- 80 x 80 mm frame
- multiple speed options
- tachometer signal available

MODEL	input voltage		input current[1]	input power[1]	rated speed[1]	airflow[2]	static pressure[3]	noise[4]
	rated (Vdc)	range (Vdc)	max (A)	max (W)	typ (RPM±10%)	(CFM)	(inch H_2O)	typ (dBA)
CFM-8025BG-140-396	12	10.8~13.2	0.27	3.24	4,000	41.40	0.27	39.6
CFM-8025BG-150-444	12	10.8~13.2	0.35	4.20	5,000	51.74	0.43	44.5
CFM-8025BG-160-484	12	10.8~13.2	0.56	6.72	6,000	62.09	0.61	48.4
CFM-8025BG-170-517	12	10.8~13.2	0.75	9.00	7,000	72.44	0.84	51.8
CFM-8025BG-240-396	24	21.6~26.4	0.15	3.60	4,000	41.40	0.27	39.6
CFM-8025BG-250-444	24	21.6~26.4	0.20	4.80	5,000	51.74	0.43	44.5
CFM-8025BG-260-484	24	21.6~26.4	0.30	7.20	6,000	62.09	0.61	48.4
CFM-8025BG-270-517	24	21.6~26.4	0.56	13.44	7,000	72.44	0.84	51.8

Notes:
1. At rated voltage, after 3 minutes.
2. At rated voltage, room temperature, 65% humidity, 0 inch H_20 static pressure.
3. At rated voltage, 0 CFM airflow.
4. Measured in an anechoic chamber as per ISO3745/GB4214-84 at rated voltage, with background noise 20±2 dBA at 1 m from the fan intake.
5. All specifications are measured at 25°C, 65% relative humidity unless otherwise specified.

Figure A.1: CUI Devices catalog.